Journal of Polymer Science and Engineering 2026, 9(1), 11915.
https://doi.org/10.24294/jpse11915

Article

A novel material model of BFRP laminated composite diaphragms for nano electro mechanical sensors

Wael A. Altabey

Department of Mechanical Engineering, Faculty of Engineering, Alexandria University, Alexandria 21544, Egypt; wael.altabey@gmail.com

CITATION

Altabey WA. A novel material model of BFRP laminated composite diaphragms for nano electro mechanical sensors. Journal of Polymer Science and Engineering. 2026; 9(1): 11915. https://doi.org/10.24294/jpse11915

ARTICLE INFO

Received: 07 November 2025
Accepted: 05 March 2026
Available online: 23 March 2026

Abstract: Understanding the mechanical properties of diaphragms is crucial for the reliability and performance of Nano Electro Mechanical Sensors (NEMS). There are various methods documented for characterizing micro materials. One well-established nondestructive approach is the bulge test, which is effective for examining the mechanical traits of diaphragms. This study aims to enhance NEMS performance by exploring how a Nano rectangular diaphragm (NRD), created from a new material within NEMS, behaves mechanically through an improved bulge test technique. The NRD is made from layers of basalt fiber reinforced polymer (BFRP) laminate composites, sized at the nanoscale, and was tested at room temperature for plane-strain bulging. Before applying any loads, the NRD is pre-stressed to eliminate any initial deflection and then securely clamped between two plates. A differential pressure is applied, causing deformation in the laminated composite NRD. This setup makes the plane-strain bulge test well-suited for analyzing the mechanical properties of the laminated composite NRD in both elastic and plastic states. We derived an exact solution to the governing equations for the symmetric cross-ply BFRP laminated composite NRD, taking into account the impact of residual strength from the pre-stressed condition. The relationship between stress and strain for the BFRP laminated composite NRD was determined through hydraulic bulging tests, and we analyzed the gradual thickness changes at different points of the hemisphere formed during the bulge test. We can also extend a finite element model (FEM) to analyze the BT outcomes and look into how pre-stress influences the pressure testing, comparing results from the FEM with those derived from analytical calculations. The relative error (E_r) for w_max between the analytical and numerical results is less than 0.336%. We ran simulations using ANSYS, MATLAB and its PDE toolbox to get our results.

Keywords: bulge test technique; mechanical behavior; micro/nano electro-mechanical sensors (MEMS/NEMS); basalt fiber reinforced polymer (BFRP)

1. Introduction

The size of the diaphragm, whether micro or nano, plays a crucial role in various engineering and bioengineering applications, like micro electro-mechanical sensors (MEMS) and Nano electro-mechanical Sensors (NEMS). For instance, pressure sensors typically feature a micro- or nano-sized diaphragm that bends when there’s a pressure difference.

Getting accurate measurements of material properties during the fabrication of both MEMS and, more recently, NEMS can be quite challenging, especially since these properties can depend on how they’re made.

Moreover, the rapid advancements in using structural elements like diaphragms at the micro and nano scales in MEMS/NEMS have created challenges in modeling these tiny structures. It’s been shown that size effects significantly impact the mechanical behavior of materials [1,2]. This emphasis on size effects has led to more focused research on the behavior of nano-structures and nano-materials [3–5].

1.2. Literature review

1.2.1. Nanofibers manufacturing

Nanofibers with diameters around 1 nanometer (nm) represent the extreme, molecular scale of fiber technology, often described as sub-nanometer or single-molecule chain fibers. These ultrathin fibers are produced using specialized techniques such as electrospinning from ultra-dilute polymer solutions, e.g., polyacrylic acid (PAA) and analyzed via Atomic Force Microscopy (AFM). Electrospinning from ultra-dilute polymer solutions is an advanced nanofabrication technique that allows for the creation of sub-nanometer fibers (SNFs), which typically have diameters below 1 nm (often reported between 0.17 and 0.63 nm) [6].

The manufacturing process can be adjusted to produce basalt fibers with diameters in the size range of 1 nm, with specialized methods like centrifugal injection or specific flame methods. The nanofillers used in manufacturing nano systems involve incorporating nanofillers-reinforced polymer matrices to significantly enhance mechanical, thermal, and electrical properties. These materials are utilized for high-performance applications in aerospace, automotive, biomedical (drug delivery), defense, and electronics, enabling the Clean Energy Sector and Power Grids, for example, improved strength and, in some cases, multifunctional, lightweight, and durable components [6].

1.2.2. Composite materials behaviors

Lately, there’s been a noticeable surge in interest and use of fiber-reinforced polymer composites in several systems. This spike is largely because they boast a fantastic strength-to-weight ratio and corrosion resistance that really outshine traditional materials like aluminum and steel. Thanks to some solid research and real-world applications, these composites have found their way into various fields, including mechanical, civil, aerospace, and automotive engineering. A lot of analytical and practical studies have been done on things like fatigue and creep damage mechanisms, as well as on durability, reliability, and how these materials perform over time in both normal and extreme conditions [1].

In the beginning, composite materials consist of three parts: the matrix, the fiber-matrix interface, and the fiber itself. They don’t all fail at the same time because they have different ultimate properties. When it comes to mechanical repeating loading, such as happens to the diaphragm in bioengineering sensors and MEMS, these materials typically go through three stages before failing. Phase I is when the matrix starts to crack, followed by Phase II, which involves local delamination that happens as the matrix cracking progresses. Finally, in Phase III, we see the actual rupture, which is the result of the consolidation of that local delamination. We can check out Figure 1 for a visual representation of this process [2].

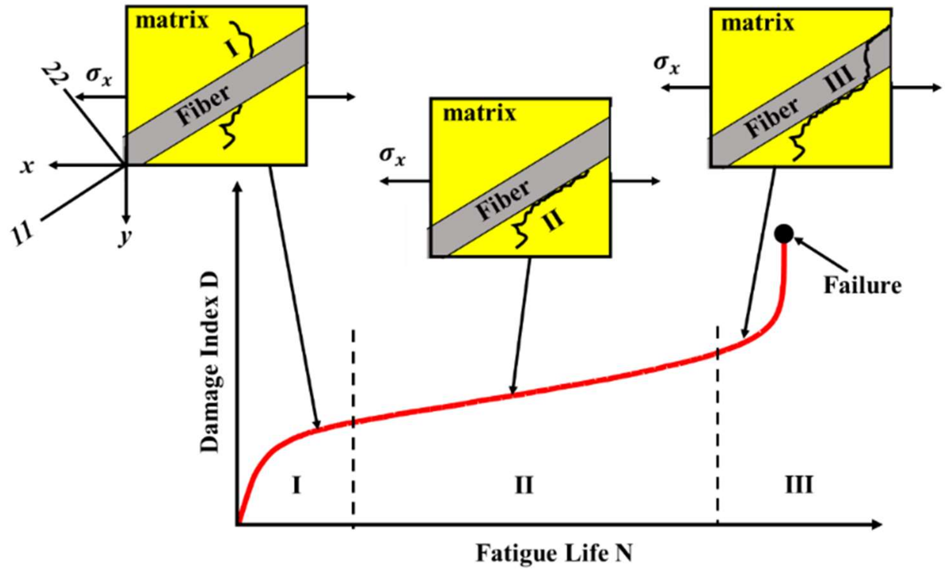

Figure 1. The failure mechanisms phases.

Understanding the failure criteria for composite materials is really important when it comes to measuring things like BT or any other sensor data. These criteria give us a way to predict when a composite structure might fail under certain loads, which is key for designing structures that can handle expected stresses and strains. Plus, they help improve the accuracy of sensors that are used to monitor potential damage.

These failure criteria also play a role in how we read sensor data for signs of damage. For example, if a composite structure experiences a load that goes beyond what we expect it to handle, a sensor can pick up on changes in strain or other metrics that suggest damage has happened. **Table A1** in **Appendix B** shows the key failure criteria.

1.2.3. The diaphragm’s behavior study

To grasp the thermomechanical behavior of nanostructures, numerous studies have been conducted on both modeling and measuring their thermomechanical characteristics, particularly under vibration and buckling loads [7–10]. The dynamic behavior of nanosized components actuated by thermal and piezoelectric means in magnetic fields has also been explored by Ebrahimi and Barati [11–13]. Piezoelectric actuators, commonly used in NEMS, have been studied under various load conditions [14,15], while the effects of shear stress on NEMS under different loads have been examined as well [16–18].

The bulge test is a well-known non-destructive method for assessing the mechanical properties of diaphragms. It allows for characterization of residual stress, elastic modulus, Poisson ratio, and other key parameters like strength and fracture toughness, all while keeping sample preparation relatively straightforward compared to other techniques. In this test, uniform pressure is applied to one side of a free-standing diaphragm, leading it to curve toward the opposite side. The relationship between the static pressure ‘P’ and the membrane deflection ‘w’ can then be used to derive mechanical properties.

That said, the accuracy of these results is heavily influenced by several potential errors related to geometry, sample holders, interferometry measurements, pressure readings, and the analytical model used in the load deflection equation. This current study aims to address these error sources to improve the analysis for new materials that haven't yet been utilized in micro/nano sensors. In particular, symmetric cross-ply BFRP laminated composites known as NRD are being tested. This material was selected because it serves as a viable and promising alternative to metals, thanks to its high stiffness-to-weight ratio, corrosion resistance, sustainability, and improved fatigue resistance and damage tolerance capabilities. Investigating this material is the main goal of the work.

1.2.4. The laminate composites test techniques

There are a couple of main ways to test laminate composites: destructive testing and non-destructive testing (NDT). Destructive testing involves various experimental methods and visual inspections on-site to evaluate samples for potential failure. This could include tests like tensile, compression, inter-laminar shear, and fracture tests. Some of the usual destructive methods for laminate composites are sectioning, bending, and fractography [19].

On the other hand, NDT techniques have been really helpful for assessing laminate composites in place, allowing us to check their structural integrity effectively [20,21]. A breakdown of the different types of NDT is shown in **Figure 2**.

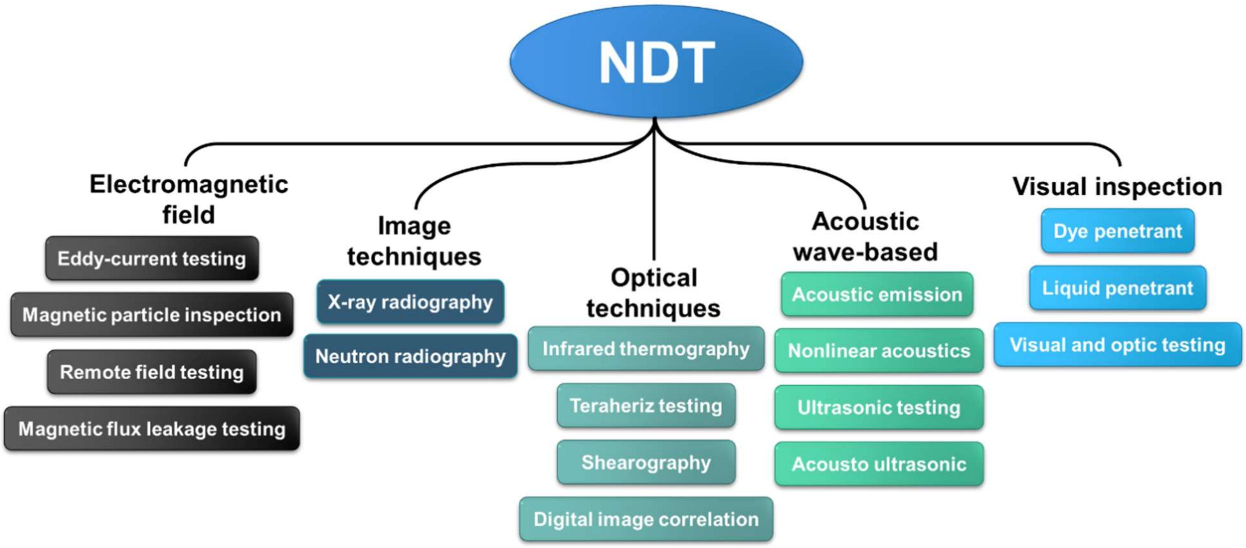

Figure 2. The different types of NDT in laminate composites.

1.2.5. Bulge test principle

The bulge test measures how a diaphragm deforms when subjected to different pressures. Figuring out the relationship between that pressure and the resulting deformation isn't straightforward.

A lot of research has been done to understand how materials behave and what characteristics they have during bulging. For instance, the first applications of this testing method were reported by Hill [22] and Mellor [23], focusing on the bulging of circular diaphragms. Chater and Neale [24], took a close look at how circular membranes act under uniform hydrostatic pressure, particularly for materials with unique plastic properties. They laid down the foundational equations for pressurized membranes. Ilahi [25] and Ilahi and Paul [26] explored how anisotropic aluminum sheets behave under hydrostatic bulging, comparing their experimental findings with theoretical predictions.

In 2017, Altabey [27] investigated how micro circular diaphragms behave thermally and mechanically using the bulge test, deriving partial differential equations (PDEs) to establish an analytical model, which showed promising alignment between finite element and analytical models.

The goal of the theoretical and numerical work so far has been to accurately predict how metals respond during hydrostatic bulging and to understand the relationships between pressure, strain, and geometric changes. Storakers [28] was among the first to apply numerical solutions to bulge tests, analyzing plastic deformation in circular membranes under one-sided hydrostatic pressure. He provided equations for stress and strain during the deformation of materials with parabolic stress-strain curves, and tackled various special cases. After that, several researchers started using numerical solutions to streamline their experimental processes, validating results from both experimental and theoretical approaches. Ahmed and Hashmi [29], examined how combined pressure and in-plane compressive loads affect sheets using the finite element method, considering the die-sheet contact conditions. They also analyzed scenarios with just pressure to compare the results. Wan et al. [30] looked at tensile residual stress in clamped plates or membranes subjected to uniform hydrostatic pressure or central loads from a cylindrical punch, deriving analytical relations based on average membrane stress and comparing them to finite element analyses. Over the last few decades, numerical solutions have become essential in the bulge test technique for determining the mechanical characteristics of metals.

Since then, research on the bulge test technique has shifted toward investigating its reliability and accuracy in assessing the mechanical properties of diaphragms. For instance, Itozaki [31] found that ignoring the initial height of membranes in analyses leads to misleading nonlinear elastic behavior of the diaphragm. Small et al. [32] studied how initial conditions like diaphragm wrinkling and residual stresses affect outcomes, using finite element analysis. Various studies have evaluated the accuracy and reliability of bulge tests [33–40]. These authors note that while determining the plane-strain modulus from the plane-strain bulge equation is generally reliable, calculating residual stress can be less satisfactory, particularly at low levels. Ultimately, some researchers have proposed approaches for analyzing bulge test data to enhance the accuracy and reliability of these techniques.

1.3. Current contribution

The plane-strain bulge test is an effective method for assessing the mechanical properties of diaphragms. In this approach, you can figure out the stress-strain curve of a diaphragm by looking at how the laminated NRD responds to pressure and deflection, as shown in **Figure 3**. When a diaphragm is in a state of plane strain, both stress and strain are evenly spread across the width of the membrane, allowing us to come up with straightforward formulas for stress and strain [41].

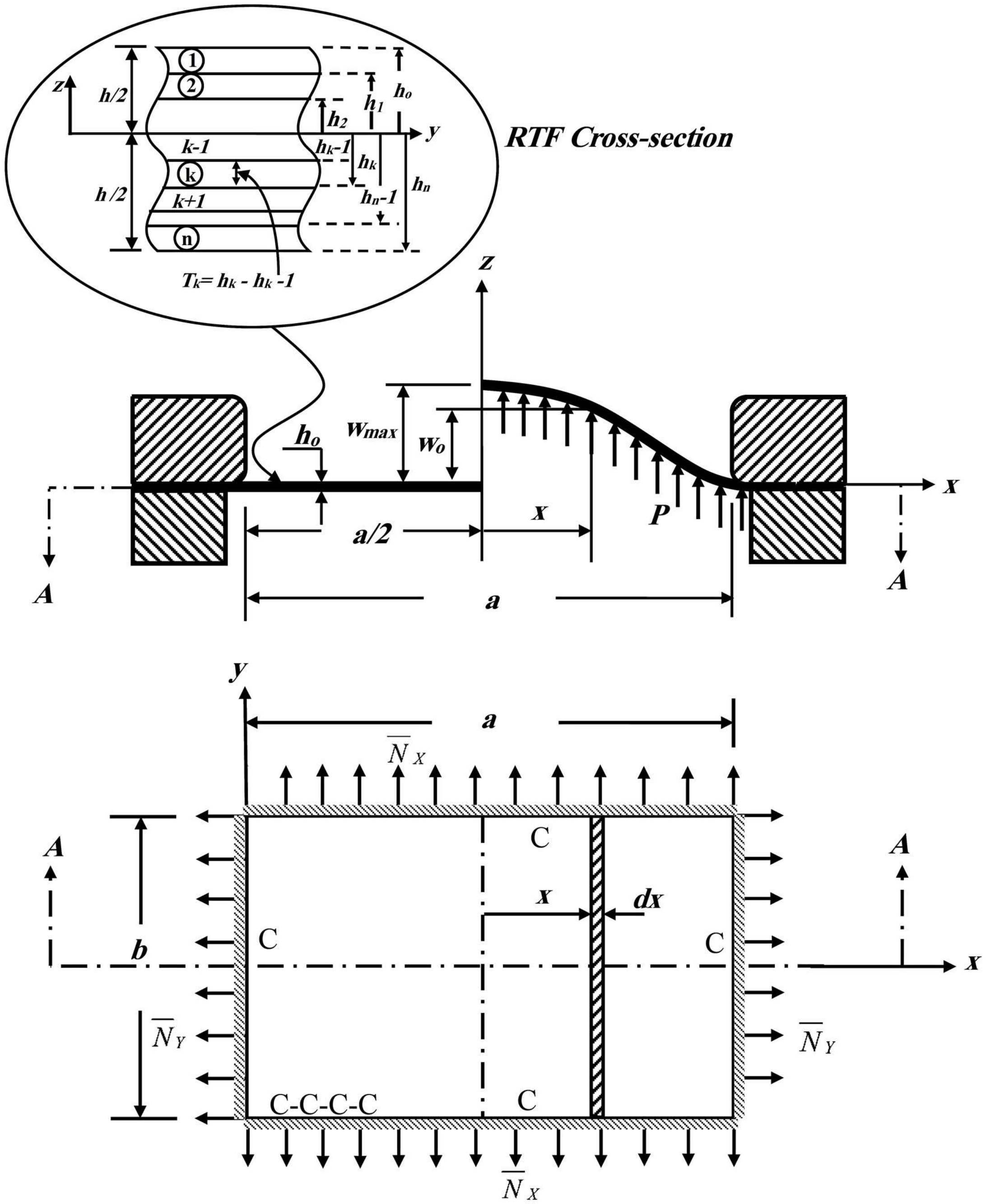

Figure 3. The geometrical model of the bulge test for the BFRP composite NRD subjected to in-plane (pre-stressed) load $\overline{N}_X$ and $\overline{N}_Y$ with clamped edges (CCCC).

3. The Bulging Test Model for NRD

3.1. Physical Model

Figure 3 shows the geometric model of the BFRP laminated composite NRD before and after deformation on both the left and right sides. In the figure, you can see that the NRD has a length in the x-direction (labeled as a) and a length in the y-direction (b), along with a thickness (h_o). Initially, the NRD is pre-stressed under a radial stress σ_0 to ensure that the initial deflection is zero before applying the load, and then it is clamped between two plates. The lower side of the diaphragm is exposed to a differential pressure (P), which causes it to deform the laminated composite NRD.

The BFRP laminate composite pipe was made up of five layers of basalt fiber arranged in the orientation $[0°/90°/0°/90°/0°]_S$, combined with a polymer resin matrix. It has a length of $100\ nm$ in the x-direction and $50\ nm$ in the y-direction, with a thickness of 1 nm for each layer. The elastic modulus values are $E_1 = 93.5$ GPa, $E_2 = E_3 = 20$ GPa, while the shear modulus values are $G_1 = G_3 = 2.35$ GPa and $G_2 = 8.5$ GPa. For the Poisson coefficients, we have $\upsilon_1 = \upsilon_3 = 0.28$ and $\upsilon_2 = 0.3$, and the overall density is $2700\ \text{kg/m}^3$, the volume fraction $V_f = 0.53$ (where the specifications of BFRP are presented in **Table 1**) [17].

Table 1. BFRP Specifications [17].

Parameter	BFRP
Fatigue Life N_f	6.12×10^4
Young's Modulus of Matrix E_m(GPa)	4.06
Volume Fraction of Matrix V_m	0.43
Young's Modulus of Fiber E_f(GPa)	97
Volume Fraction of Fiber V_f	0.53
Young's Modulus of Composite E_c(GPa)	92
Polymer Melting Point T_m(°K)	446
Fiber-Matrix Interface Strength f^*	0.52
fatigue stress S_f(MPa)	137
Ultimate Tensile Stress S_{ult}(MPa)	1409
Minimum Fatigue Stress σ_{min}(MPa)	14.2
Maximum Fatigue Stress σ_{max}(MPa)	139
Stress Ratio R	0.10
Percentage of Drop in Stiffness n	1.66

3.2. Mathematical Model

3.2.1. The Assumption

1. The displacements in the x and y directions i.e. u_o and v_o are very small so we can be neglected and the effective equation that is the equation at the direction of the deflection w_o.
2. The steady state condition, so we can be neglected the change of deflection w_o with the time t.
3. The pre-stressed rectangular thin plate in the hydraulic bulge system the in-plane Load are in x and y direction only i.e. $\overline{N}_{XY} = 0$.
4. The plate with thickness h subjected to uniform pressure load P.
5. The plate is symmetric cross-ply laminates.

It is known that classical Laminated Plate Theory (CLPT) cannot be applied directly to nano-sized plates in its original, local form, while the CLPT is an effective, simple approach for thin, macro-scale, composite laminated structures, it fails at the nanoscale because it ignores small-scale (size-dependent) effects, which are critical at that level. To make CLPT applicable to nano-sized plates, it must be modified to include nonlocal continuum mechanics by adding the nonlocal elasticity theory, which is integrated into the governing equations of CLPT to account for small-scale effects. Where in nonlocal continuum mechanics, the stress at a specific point in the nanoplate is not just a function of the strain at that point (local), but a function of the strains of all points in the entire body. The governing equations are modified by incorporating a nonlocal parameter ($\mu\nabla^2$) (**Appendix A.1.1.**) that represents the internal length scale (atomic distances), making the analysis size-dependent. The derivation of governing PDE in current laminated NRD including nonlocal elasticity theory are presented in **Appendix A**, herein, the results of derivation are become:

$$\psi_1 W_{xxxx} + 2\psi_2 W_{xxyy} + W_{yyyy} + \mu\alpha_1 W_{xx} + \mu\alpha_2 W_{yy} = \overline{P} \tag{1}$$

where: $\psi_1 = \frac{D_{11}}{D_{22}}$, $\psi_2 = \frac{(D_{12} + 2D_{66})}{D_{22}}$, $\alpha_1 = \frac{\overline{N}_X}{D_{22}}$, $\alpha_2 = \frac{\overline{N}_Y}{D_{22}}$, $\overline{P} = \frac{P}{D_{22}}$, D_{ij} is the diaphragm's flexural rigidity, μ is the nonlocal parameter,.

The maximum deflection (see **Appendix A**) is obtained at the diaphragm center ($x = a/2$ and $y = 0$), where:

$$w_{\max} = \mu \sum_{m=1,3,5,\cdots}^{\infty} \gamma_m (-1)^{\frac{m-1}{2}} \left[\left(\frac{-\phi_m \tanh^2(\phi_m)}{(\phi_m \cosh(\phi_m) + \sinh(\phi_m) - \phi_m \tanh(\phi_m)\sinh(\phi_m)))} - \frac{1}{\cosh(\phi_m)} \right) + 1 \right] \tag{2}$$

Let's take a look at a basic parallelepiped shape cut from the diaphragm, as illustrated in **Figure 4**. We're going to consider positive internal forces and moments acting on the nearer faces of this diaphragm element.

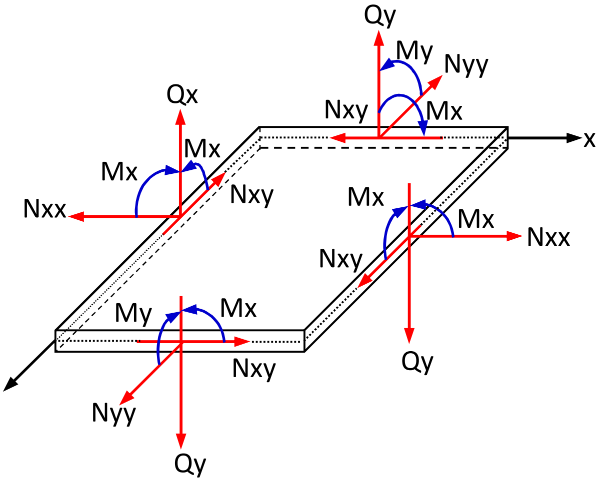

Figure 4. The shear forces and moments on a laminate.

For the bending moment M_x, M_y and M_{xy} (see **Appendix A**) may thus be expressed:

$$\begin{aligned} M_X = \mu \sum_{m=1,3,5,\cdots}^{\infty} \Bigg[& B_m \left(D_{11} \left(\frac{m\pi}{a} \right)^2 - D_{12} \left(\frac{2\phi_m}{b} \right)^2 \right) \cosh\left(\frac{2\phi_m y}{b} \right) + D_{11} \left(\frac{m\pi}{a} \right)^2 \gamma_m + C_m \Bigg(D_{11} \left(\frac{m\pi}{a} \right)^2 \\ & - D_{12} \left(\frac{2\phi_m}{b} \right)^2 \Bigg) \left(\frac{2\phi_m y}{b} \right) \sinh\left(\frac{2\phi_m y}{b} \right) - 2C_m D_{12} \left(\frac{2\phi_m}{b} \right)^2 \cosh\left(\frac{2\phi_m y}{b} \right) \Bigg] \sin\left(\frac{m\pi x}{a} \right) \end{aligned} \tag{3}$$

$$\begin{aligned} M_Y = \mu \sum_{m=1,3,5,\cdots}^{\infty} \Bigg[& B_m \left(D_{12} \left(\frac{m\pi}{a} \right)^2 - D_{22} \left(\frac{2\phi_m}{b} \right)^2 \right) \cosh\left(\frac{2\phi_m y}{b} \right) + D_{12} \left(\frac{m\pi}{a} \right)^2 + C_m \Bigg(D_{12} \left(\frac{m\pi}{a} \right)^2 \\ & - D_{22} \left(\frac{2\phi_m}{b} \right)^2 \Bigg) \left(\frac{2\phi_m y}{b} \right) \sinh\left(\frac{2\phi_m y}{b} \right) - 2C_m D_{22} \left(\frac{2\phi_m}{b} \right)^2 \cosh\left(\frac{2\phi_m y}{b} \right) \Bigg] \sin\left(\frac{m\pi x}{a} \right) \end{aligned} \tag{4}$$

$$M_{XY} = \mu \sum_{m=1,3,5,\cdots}^{\infty} D_{66} \frac{m\pi}{a} \frac{4\phi_m}{b} \left[-B_m \sinh\left(\frac{2\phi_m y}{b} \right) - C_m \left(\left(\frac{2\phi_m y}{b} \right) \cosh\left(\frac{2\phi_m y}{b} \right) + \sinh\left(\frac{2\phi_m y}{b} \right) \right) \right] \cos\left(\frac{m\pi x}{a} \right) \tag{5}$$

where, μ is the nonlocal parameter, for shear force Q_x and Q_y (see **Appendix A**) may thus be expressed:

$$\begin{aligned} \therefore Q_X = \mu \sum_{m=1,3,5,\cdots}^{\infty} \Bigg[& B_m \frac{m\pi}{a} \left(D_{11} \left(\frac{m\pi}{a} \right)^2 - (D_{12} + 4D_{66}) \left(\frac{2\phi_m}{b} \right)^2 \right) \cosh\left(\frac{2\phi_m y}{b} \right) \\ & C_m \frac{m\pi}{a} \left(D_{11} \left(\frac{m\pi}{a} \right)^2 - (D_{12} + 4D_{66}) \left(\frac{2\phi_m}{b} \right)^2 \right) \left(\frac{2\phi_m y}{b} \right) \sinh\left(\frac{2\phi_m y}{b} \right) + D_{11} \left(\frac{m\pi}{a} \right)^3 \gamma_m \\ & - 2C_m (D_{12} + 4D_{66}) \frac{m\pi}{a} \left(\frac{2\phi_m}{b} \right)^2 \cosh\left(\frac{2\phi_m y}{b} \right) \Bigg] \cos\left(\frac{m\pi x}{a} \right) \end{aligned} \tag{6}$$

$$\begin{aligned} \therefore Q_Y = \mu \sum_{m=1,3,5,\cdots}^{\infty} \Bigg[& B_m \frac{2\phi_m}{b} \left((D_{12} + 4D_{66}) \left(\frac{m\pi}{a} \right)^2 - D_{22} \left(\frac{2\phi_m}{b} \right)^2 \right) \sinh\left(\frac{2\phi_m y}{b} \right) \\ & + C_m \frac{2\phi_m}{b} \left((D_{12} + 4D_{66}) \left(\frac{m\pi}{a} \right)^2 - D_{22} \left(\frac{2\phi_m}{b} \right)^2 \right) \left(\frac{2\phi_m y}{b} \right) \cosh\left(\frac{2\phi_m y}{b} \right) \\ & C_m \left((D_{12} + 4D_{66}) \left(\frac{m\pi}{a} \right)^2 \frac{2\phi_m}{b} - 3D_{22} \left(\frac{2\phi_m}{b} \right)^3 \right) \sinh\left(\frac{2\phi_m y}{b} \right) \Bigg] \sin\left(\frac{m\pi x}{a} \right) \end{aligned} \tag{7}$$

where, μ is the nonlocal parameter, the maximum stresses σ_x, σ_y and τ_{xy} take place on the surfaces $Z = \pm h/2$ (see **Appendix A**), may thus be expressed:

$$\begin{aligned} \sigma_X = \mu \sum_{m=1,3,5,\cdots}^{\infty} \frac{12}{h^3} Z \Bigg[& B_m \left(D_{12} \left(\frac{m\pi}{a} \right)^2 - D_{22} \left(\frac{2\phi_m}{b} \right)^2 \right) \cosh\left(\frac{2\phi_m y}{b} \right) + D_{12} \left(\frac{m\pi}{a} \right)^2 + C_m \Bigg(D_{12} \left(\frac{m\pi}{a} \right)^2 \\ & - D_{22} \left(\frac{2\phi_m}{b} \right)^2 \Bigg) \left(\frac{2\phi_m y}{b} \right) \sinh\left(\frac{2\phi_m y}{b} \right) - 2C_m D_{22} \left(\frac{2\phi_m}{b} \right)^2 \cosh\left(\frac{2\phi_m y}{b} \right) \Bigg] \sin\left(\frac{m\pi x}{a} \right) \end{aligned} \tag{8}$$

$$\sigma_Y = \mu \sum_{m=1,3,5,\cdots}^{\infty} \frac{12}{h^3} Z \left[B_m \left(D_{12}\left(\frac{m\pi}{a}\right)^2 - D_{22}\left(\frac{2\phi_m}{b}\right)^2 \right) \cosh\left(\frac{2\phi_m y}{b}\right) + D_{12}\left(\frac{m\pi}{a}\right)^2 + C_m \left(D_{12}\left(\frac{m\pi}{a}\right)^2 \right.\right.$$
$$\left.\left. - D_{22}\left(\frac{2\phi_m}{b}\right)^2 \right)\left(\frac{2\phi_m y}{b}\right) \sinh\left(\frac{2\phi_m y}{b}\right) - 2C_m D_{22}\left(\frac{2\phi_m}{b}\right)^2 \cosh\left(\frac{2\phi_m y}{b}\right) \right] \sin\left(\frac{m\pi x}{a}\right) \tag{9}$$

$$\tau_{XY} = \mu \sum_{m=1,3,5,\cdots}^{\infty} \frac{12}{h^3} Z D_{66} \frac{m\pi}{a} \frac{4\phi_m}{b} \left[-B_m \sinh\left(\frac{2\phi_m y}{b}\right) - C_m \left(\left(\frac{2\phi_m y}{b}\right) \cosh\left(\frac{2\phi_m y}{b}\right) + \sinh\left(\frac{2\phi_m y}{b}\right) \right) \right] \cos\left(\frac{m\pi x}{a}\right) \tag{10}$$

where, μ is the nonlocal parameter, for the strain ε_x, ε_y and γ_{xy} (see **Appendix A**) may thus be expressed:

$$\varepsilon_X = -z\mu\left(\frac{m\pi}{a}\right)^2 \left[-B_m \cosh\left(\frac{2\phi_m y}{b}\right) - C_m \left(\frac{2\phi_m y}{b}\right) \sinh\left(\frac{2\phi_m y}{b}\right) - \gamma_m \right] \sin\left(\frac{m\pi x}{a}\right) \tag{11}$$

$$\varepsilon_Y = -z\mu\left(\frac{2\phi_m}{b}\right)^2 \left[B_m \cosh\left(\frac{2\phi_m y}{b}\right) + C_m \left(\left(\frac{2\phi_m y}{b}\right) \sinh\left(\frac{2\phi_m y}{b}\right) + 2\cosh\left(\frac{2\phi_m y}{b}\right) \right) \right] \sin\left(\frac{m\pi x}{a}\right) \tag{12}$$

$$\gamma_{XY} = -z\mu \frac{4m\pi\phi_m}{ab} \left[B_m \sinh\left(\frac{2\phi_m y}{b}\right) + C_m \left(\left(\frac{2\phi_m y}{b}\right) \cosh\left(\frac{2\phi_m y}{b}\right) + \sinh\left(\frac{2\phi_m y}{b}\right) \right) \right] \cos\left(\frac{m\pi x}{a}\right) \tag{13}$$

where, μ is the nonlocal parameter.

3.2.2. The laminate NRD thickness distribution

The membrane theory is often applied to figure out the flow stress curve using the bulge test [42,43], as shown in **Figure 5**. This theory tends to ignore bending stresses through the thickness of the diaphragm, so it mainly works for diaphragms. For the bulge test, it provides a specific relationship between stress, strain, and diaphragm geometry. Let's look at how this applies to free forming of a laminated diaphragm. The current half arc length of any meridian that goes through the dome's apex is denoted as Rα, where R is the radius of the dome and α is half the angle formed by the dome's surface at the center of curvature (again, see **Figure 5**). The initial half arc length for the meridian in question is a, which means it's stretched $2R\alpha/a = \alpha/\sin\alpha$ a certain times. Given the symmetry, we can conclude that the main positive strains are equal to one another, and the thickness at the dome's apex will be equal as well.

$$h_d = h_0\left(\frac{\sin\alpha}{\alpha}\right)^2 \tag{14}$$

Because the clamp stays intact during the forming process, there's hardly any deformation around the edges. However, the area closer to the edges gets stretched quite a bit $\alpha/\sin\alpha$, which leads us to conclude that the thickness of the dome at the edges is:

$$h_P = h_0\left(\frac{\sin\alpha}{\alpha}\right) \tag{15}$$

At a certain point during the deformation, point M shifts to point M', and point O moves to O', as illustrated in **Figure 5**. Let's denote Ψ as the angle between the symmetry axis and the dome radius that connects to point M'. The latitude that goes through point M' gets stretched by a certain factor, and you can determine the dome thickness at point M' with the following method:

$$h = h_0\left(\frac{x}{x_0}\right)\left(\frac{sin\,\alpha}{\alpha}\right) \tag{16}$$

Taking into account that $x = R\,sin\,\Psi$, $x_0 = ca/2$ and $\Psi = c\alpha$ the dome thickness at any point could be calculated from the following Equation (15):

$$h = h_0\left(\frac{\Psi}{sin\,\Psi}\right)\left(\frac{sin\,\alpha}{\alpha}\right)^2 \tag{17}$$

The radius of curvature, see **Figure 5**, is:

$$R = \frac{a^2 + w_{\max}}{2w_{\max}},\ \alpha = \sin^{-1}\left(\frac{a}{R}\right),\ \Psi = \tan^{-1}\left(\frac{x}{S}\right) \text{ and } S = \frac{a}{\tan\alpha}$$

You can determine the dome thickness at any point using Equation (17), which takes into account the values of (a, w_{max}, h_0, x):

$$\frac{h}{h_0} = \left(\frac{\mu_1}{\mu_2}\right)^2\left(\frac{\mu_3}{\mu_4}\right) \tag{18}$$

where: $\mu_1 = \frac{2aw_{\max}}{\left(a^2 + w_{\max}\right)}$, $\mu_2 = \sin^{-1}(\mu_1)$, $\mu_3 = \tan^{-1}\left(\frac{x}{a}\tan(\mu_2)\right)$, $\mu_4 = \sin(\mu_3)$

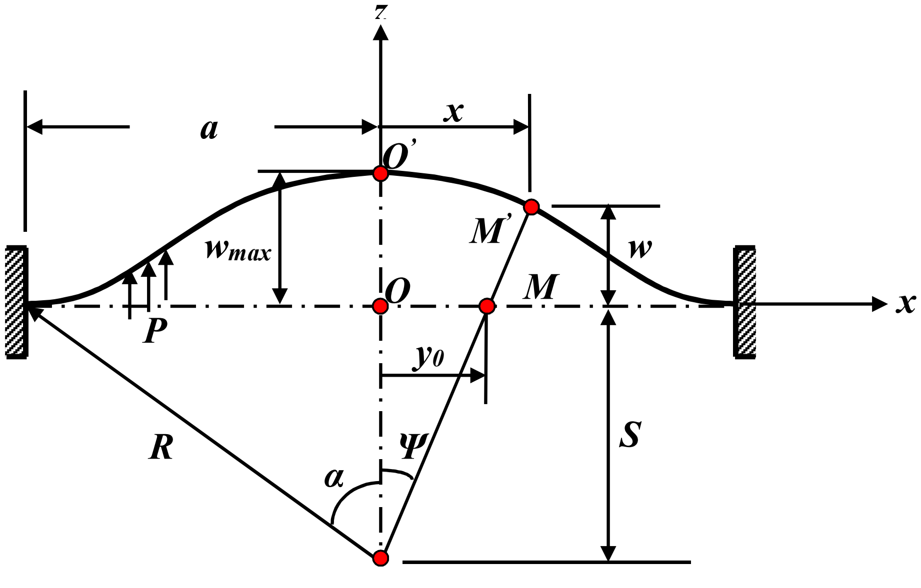

Figure 5. Schematic of deformation modeling.

4. Results and discussion

Figures 6–9 show how the NEMS material behaves mechanically, we can see a typical example of Nano-deformation, which includes deflection and strain, for a NRD with geometrical and physical properties as shown in **Section 3.1**.

4.1. Convergence study and accuracy

In this section, we look into how well the proposed method converges. We calculate the residual stress, σ_0, and Young's modulus using the technique we've presented, and then we compare these results with what's already out there in the literature. You can see a convergence and comparison study for Si_3N_4 diaphragms in **Table 2**. Silicon nitride (Si_3N_4) is commonly used in MEMS devices because of its excellent chemical and mechanical properties.

We compare our computational results with existing values from previous studies [44–46]. We found that our results match up quite closely.

Table 2. Convergence study of the residual stress σ0 and Young's modulus of the Si_3N_4 diaphragms.

	Tabata et al. [44]	**Present**	**Vlassak and Nix [45]**	**Present**	**Edwards et al. [46]**	**Present**
Residual stress σ_0	1 GPa	0.965 GPa	150 MPa	147.82 MPa	130 MPa	127.78 MPa
Young's modulus	290 GPa	287.8 GPa	222 GPa	221 GPa	258 GPa	255.6 GPa

4.2. BFRP nano rectangular diaphragm (NRD)

In **Figure 6**, you can see that the transverse Nano-deflection wo increases as the NRD longitudinal distance (a) along the x-direction goes up, while it decreases when the NRD lateral distance (b) along the y-direction increases. The highest Nano-deflection of $w_{max} = 7.0527$ nm occurs at a pressure of 10 Pa at the center of the NRD, specifically when $a = a/2$ and $b = 0$.

Figures 7–9 illustrate that the distributions of Nano-strain, namely ε_x, ε_y and γ_{xy} (in nm/nm), are symmetric in both the longitudinal and lateral directions. This symmetry means that the strain behavior in one quarter of the NRD mirrors that of the corresponding quarter along the NRD axis. The peak Nano-strain values of ε_x, ε_y and γ_{xy} are 0.43504, 0.53257 and 0.38729 (nm/nm), respectively, and these occur at a pressure of 10 Pa.

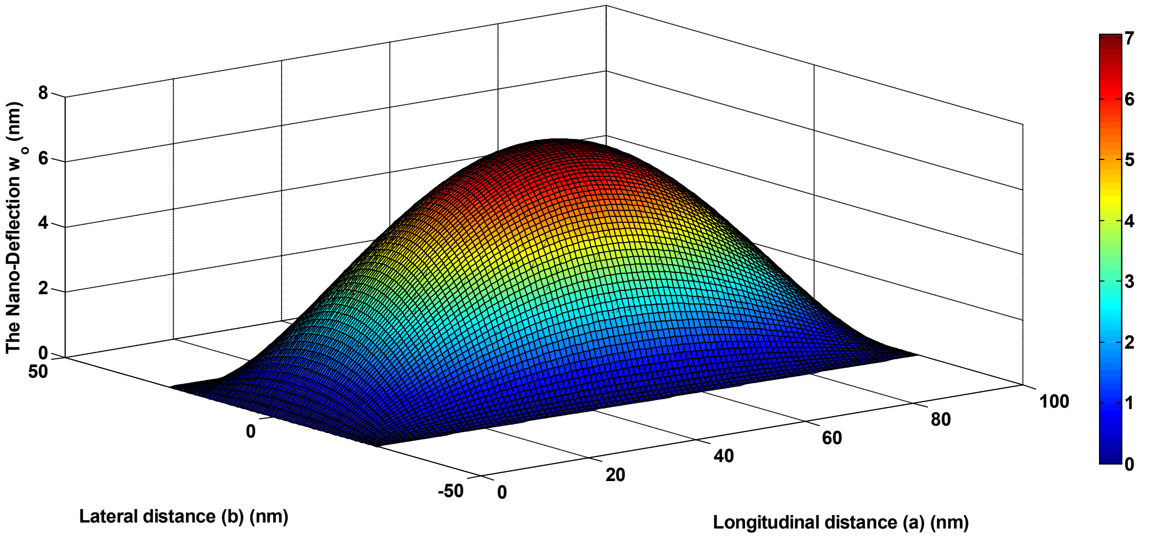

Figure 6. The 3D Nano-deflection distribution along NRD for BFRP composite material with $[0°/90°/0°/90°/0°]_S$ laminate layer angle.

In **Figure 7**, we see that the Nano-strain ε_x goes up as the NRD longitudinal distance (a) increases along the x-direction, but it decreases when the NRD lateral distance (b) increases along the y-direction. The highest Nano-strain ε_x actually occurs right in the center of the NRD when at $a = a/2$ and $b = 0$.

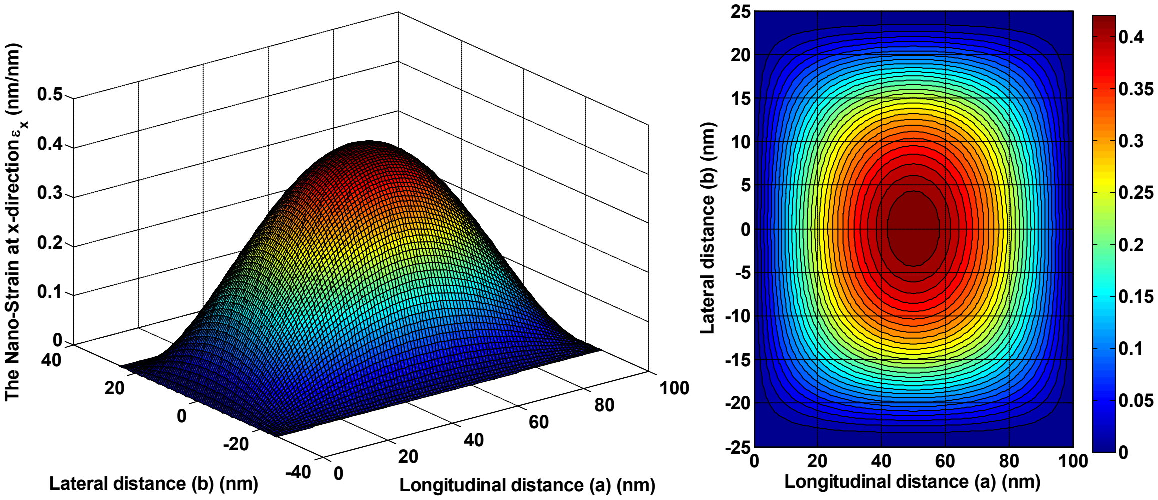

Figure 7. Nano-strain ε_x (nm/nm) distribution along NRD for the BFRP composite material with $[0°/90°/0°/90°/0°]_S$ laminate layer angle, contour profile at right and 3D profile at left.

On the other hand, in **Figure 8**, the Nano-strain ε_y is zero (nm/nm) across most of the NRD surface, except for the ends of the diaphragm. Here, ε_y increases with an increase in the NRD longitudinal distance (a) along the x-direction at both ends, with the peak value happening at the center edge of the NRD when $a = a/2$ and $b = \pm b/2$. But, at the other edges along the y-direction, the Nano-strain ε_y remains at zero (nm/nm).

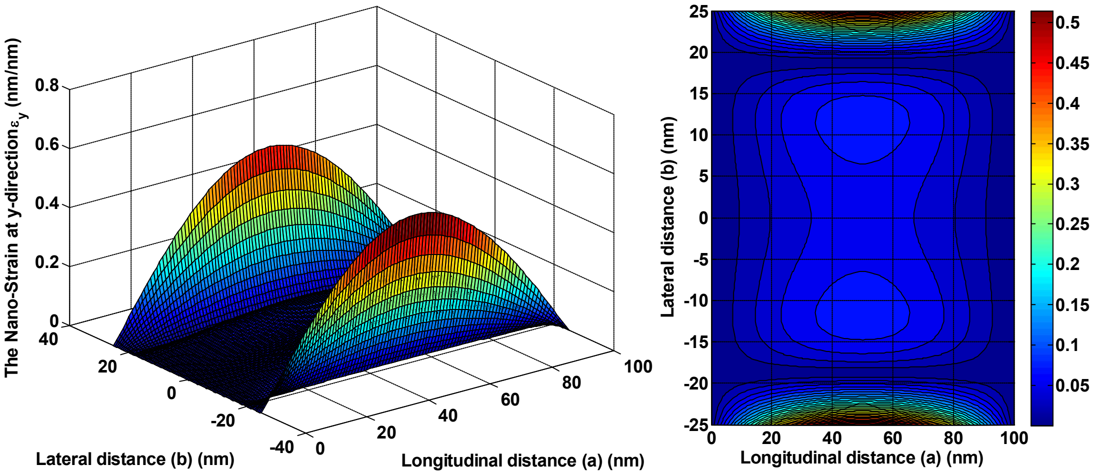

Figure 8. Nano- strain ε_y (nm/nm) distribution along NRD for the BFRP composite material with $[0°/90°/0°/90°/0°]_S$ laminate layer angle, contour profile at right and 3D profile at left.

In **Figure 9**, you can see that the Nano-strain γ_{xy} is zero (nm/nm) right at the center of the NRD when $a = a/2$ and $b = 0$. As you move along the longitudinal distance (a) in the x-direction starting from $a = a/2$, the Nano-strain γ_{xy} drops from its maximum to zero (nm/nm), and then it actually rises back to its peak. On the flip side, as the lateral distance (b) in the y-direction increases, the Nano-strain γ_{xy} grows from zero (nm/nm) to its maximum, and then it decreases back to zero. The highest values of Nano-strain γ_{xy} are found near the four edges of the NRD at $a = 0, a$ and $b = \pm b/4$.

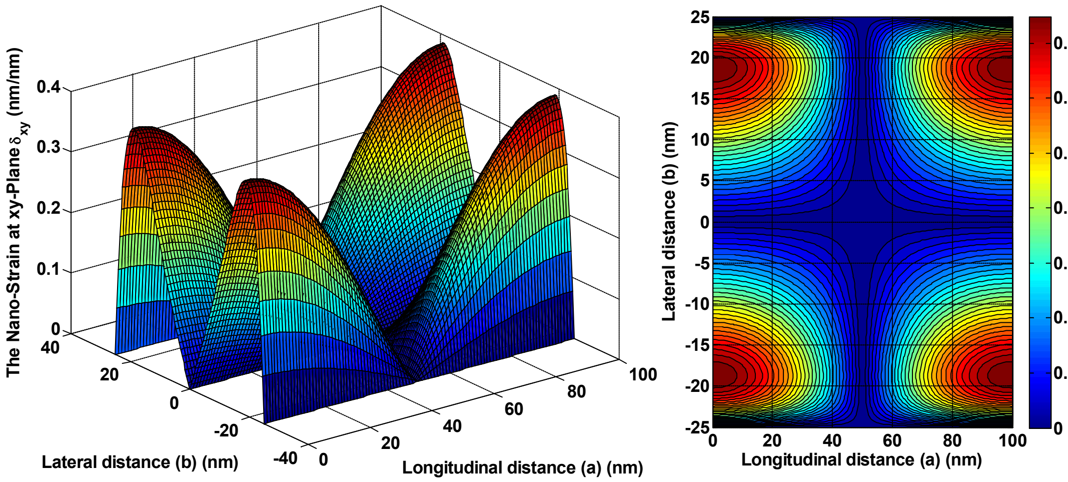

Figure 9. Nano-strain γ_{xy} (nm/nm) distribution along NRD for the BFRP composite material with $[0°/90°/0°/90°/0°]_S$ laminate layer angle, contour profile at right and 3D profile at left.

Figure 10 shows how stress is distributed across the thickness of the NRD in the contour profile. You can see that the stress is balanced on both sides of the midplane. Above the midplane, there's tension, while below it, the material experiences compression. Both areas see a maximum stress of about ± 3.637 Pa at a pressure of 10 Pa, and right at the midplane, the stress is zero.

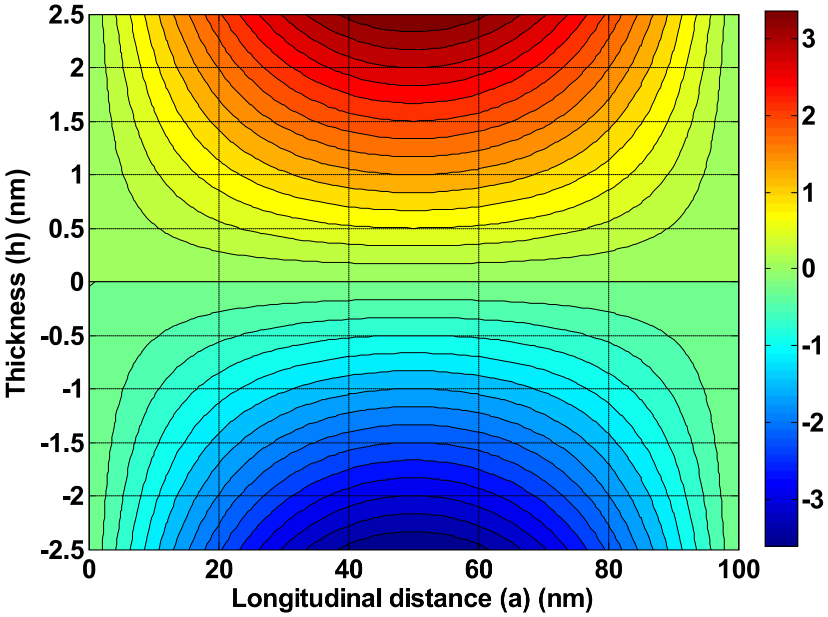

Figure 10. The stress distribution across the NRD thickness in the contour profile.

In **Figure 11**, we adjusted the differential pressure from 10 to 25 Pa in increments of 5 Pa. This was done to measure the transverse Nano-deflection wo. As the figure indicates, as we ramped up the pressure (P), the transverse Nano-deflection wo went up, with the maximum Nano-deflection w_{max} ranging between 7.0527 and 28.21 nm.

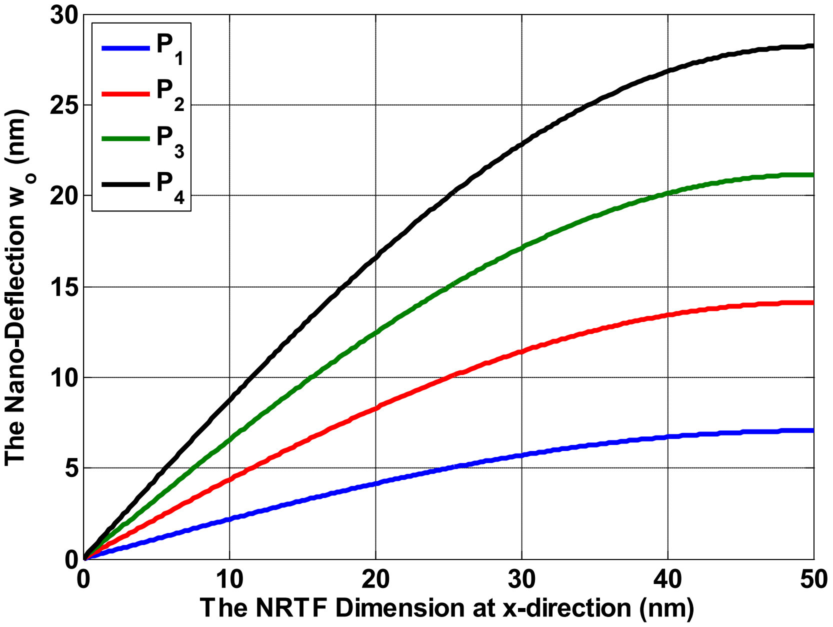

(**a**) Longitudinal Distance

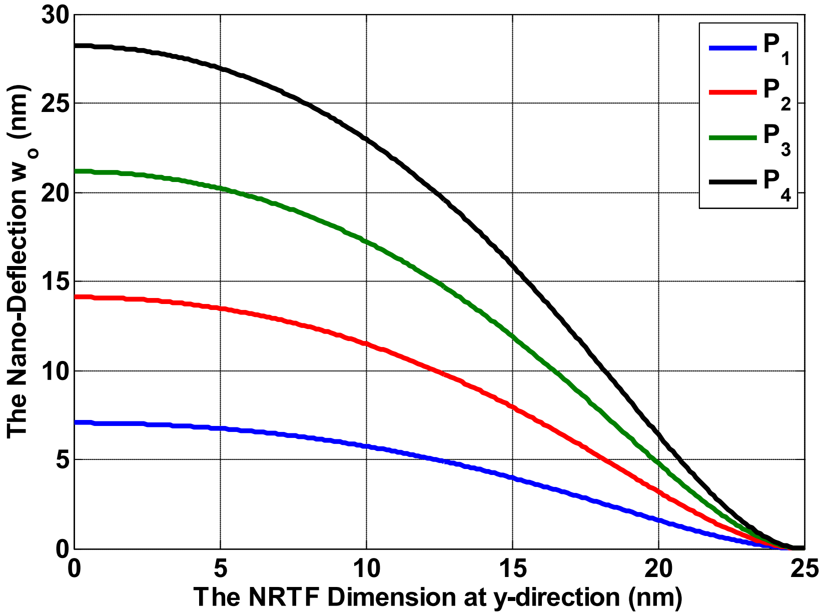

(**b**) Lateral Distance

Figure 11. Nano-Deflection profile with differential pressure of NRD for BFRP composite material with $[0°/90°/0°/90°/0°]_S$ laminate layer angle.

Figures 12 and 13 illustrate how stress relates to the Namo-strain of NRD when the differential pressure varies between 10 and 25 Pa, going up in increments of 5 Pa.

Looking at **Figures 12 and 13**, it's clear that as stress and pressure (P) increase, the Nano-strain rises as well. The maximum Nano-strain ranges from 0.43504 to 1.74 (nm/nm) for ε_x, and from 0.06177 to 0.2465 (nm/nm) for ε_x and ε_y respectively. This relationship is crucial for engineering analysis since we can determine the Young's modulus E of the NRD material based on the slope of this linear relationship $E = \Delta\sigma/\Delta\varepsilon$. Consequently, we can express Young's modulus E, which came out to be 42.01 GPa for E_x and 58.63 GPa for E_x and E_y.

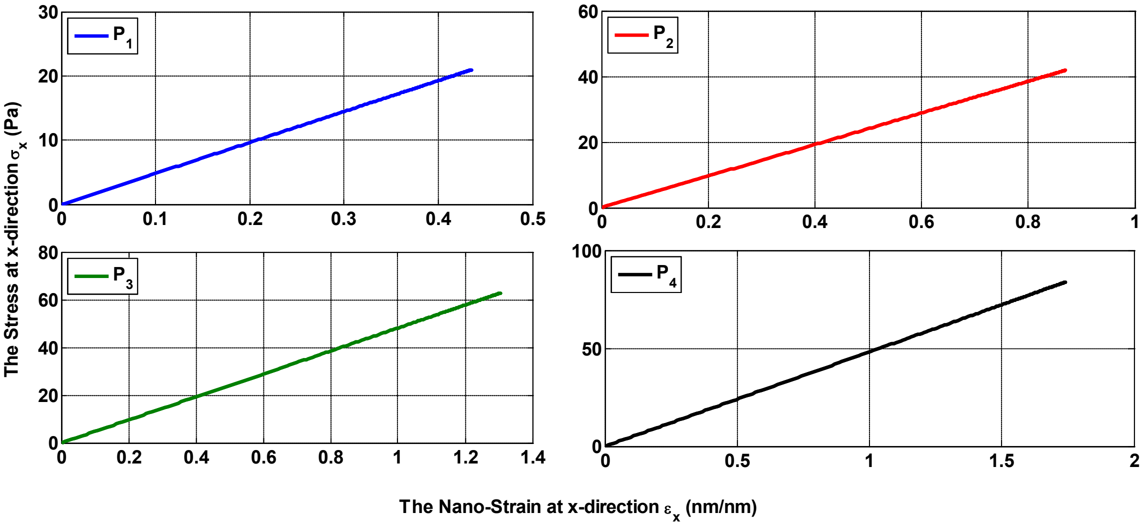

Figure 12. Stress and Namo-strain relationship at x-direction with differential pressure of NRD for BFRP composite material with $[0°/90°/0°/90°/0°]_S$ laminate layer angle.

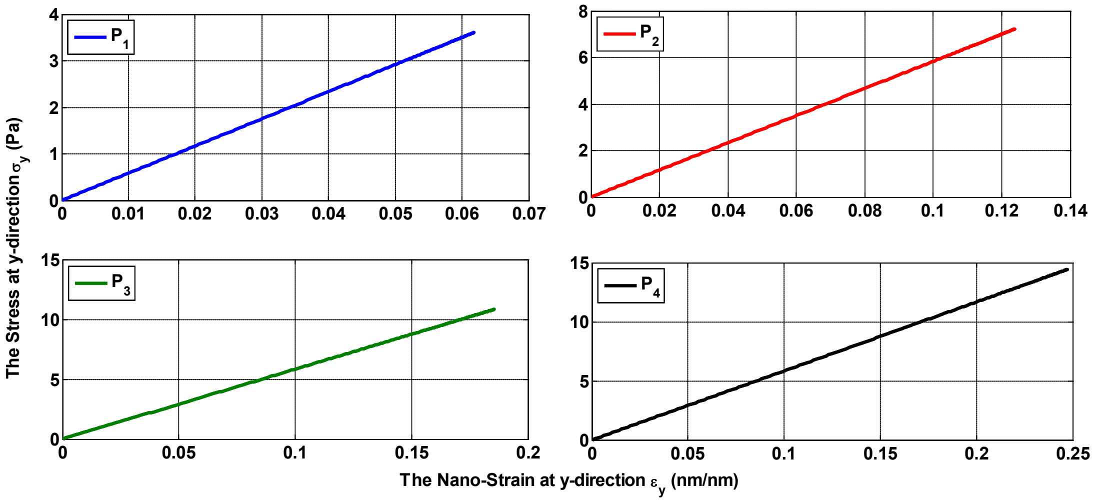

Figure 13. Stress and Namo-strain relationship at y-direction with differential pressure of NRD for BFRP composite material with $[0°/90°/0°/90°/0°]_S$ laminate layer angle.

Understanding how the Nano-thickness deformation behaves in the NRD is crucial for enhancing its mechanical properties, especially to ensure the diaphragm can endure bulging loads, which is key for NEMS reliability.

In **Figure 14**, you can see how the Nano-thickness changes with pressure variations. The thickness (h) drops from 5 to 4.883 nm as the pressure (P) goes up from 0 to 10 Pa in both directions. At the same time, the Nano-strain (ε_h) increases as the applied pressure rises in both directions.

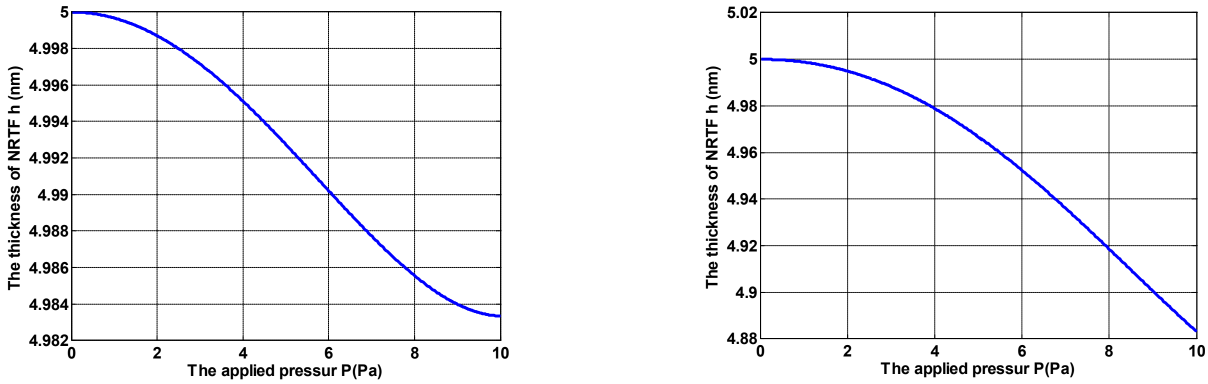

(**a**) P vs. h at x-direction (**b**) P vs. h at y-direction

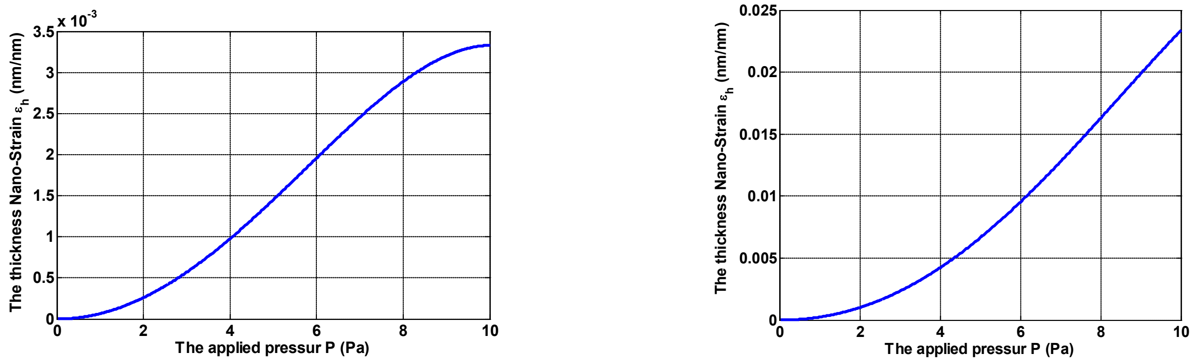

(**c**) P vs. ε_h at x-direction (**d**) P vs. ε_h at y-direction

Figure 14. The relation between differential pressure (P) and the thickness nano-deformation of NRD for the BFRP composite material with $[0°/90°/0°/90°/0°]_S$ laminate layer angle.

Figure 15 illustrates how the NRD deforms under a pressure of $P = P_1 = 10$Pa numerically using ANSYS software (ANSYS 14), showing the 3D contour mode. From the figure, we can see that the highest deflection happens at $a = a/2$ and $b = 0$, where the maximum deflection w_{max} reaches 7.1 nm. When we compare the maximum deflection from the FEM to the results from analytical calculations, we notice they're quite close.

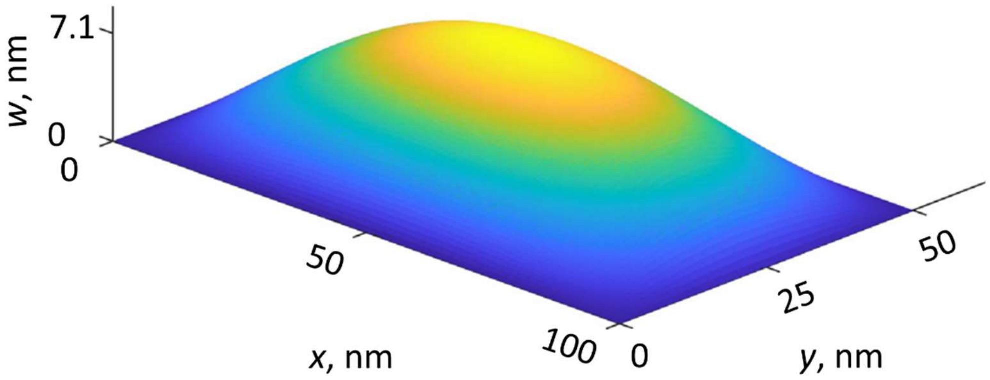

Figure 15. The diaphragm 3D deformation.

4.3. Accuracy and reliability evaluation of the current analysis for NRD

To calculate the error between analytical and numerical results to evaluate the accuracy and reliability of the current analysis for NRD, we primarily use two metrics: absolute error and relative error. These methods quantify how close the numerical solution is to the true analytical solution.

The absolute error measures the raw numerical difference between the true value and the approximate value. It provides the magnitude of the error in the same units as the measured quantity, like this:

$$E_a = \left|X_{analytical} - X_{numerical}\right| \tag{19}$$

where $X_{analytical}$ is the analytical solution and $X_{numerical}$ is numerical solution.

The relative error provides a better sense of the error's significance by comparing the absolute error to the size of the true value. It is a dimensionless value and is often expressed as a percentage (percentage error), like this:

$$E_r = \frac{\left|X_{analytical} - X_{numerical}\right|}{\left|X_{analytical}\right|} \times 100 \tag{20}$$

Figure 16 presents the relative error (E_r) between analytical and numerical results, the relative error is less than 0.336% for w_{max} between analytical and numerical results, therefore, the present analysis for NRD gave a good agreement for the numerical results, even for w_{max} of NRD.

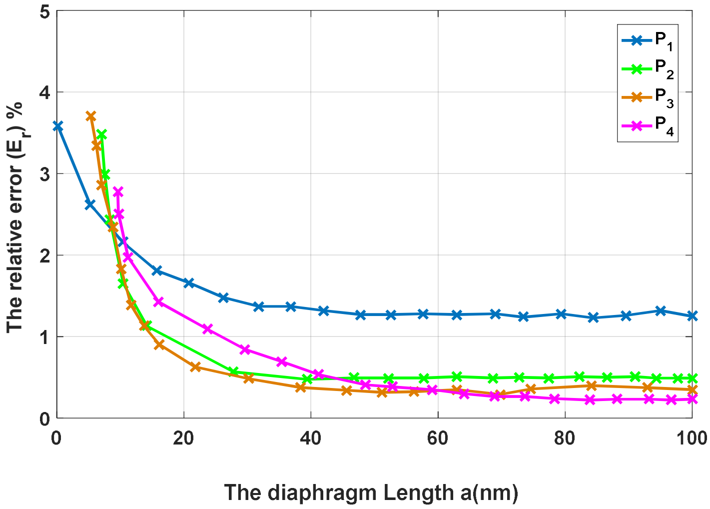

Figure 16. The relative error (E_r) between analytical and numerical results under various pressures (P).

5. Conclusion

This study uses bulging tests to explore the mechanical properties of Nano rectangular diaphragms (NRD) found in Nano Electro Mechanical Sensors (NEMS), specifically those made from basalt fiber reinforced polymer (BFRP) composite materials. These Nano-diaphragms are already used as mechanical actuators for coplanar waveguides within the nanometer wavelength range. The next step involves leveraging the elastic behavior of these diaphragms by utilizing electrostatic forces to move them. We've established the exact solutions to the governing equations for laminated NRD. The relationships regarding the mechanical properties of the NRD material have been plotted and analyzed. We also discussed the thickness distribution across the nano-diaphragm to understand its durability under deformation from differential pressure (P). As a result, this technique has developed to a point where it's become a reliable and efficient tool for determining mechanical characteristics. We calculated the Young's moduli, E_x and E_y, to be 42.01 and 58.63 GPa respectively for the Nano-diaphragm material with a thickness of $5\ nm$. The maximum Nano-deflection, w_{max}, was estimated at 7.0527 nm, occurring at the center of the NRD. In bulging tests conducted at an applied pressure of $10\ Pa$, the strain at the center of the NRD was found to be 0.43504 (nm/nm). The stress across the NRD thickness was estimated to be ± 3.637 Pa—tension above the midplane and compression below it. Notably, the NRD thickness decreased from 5 to 4.883 nm as the applied pressure (P) rose from 0 to $10\ Pa$. A comparison was made between the two methods to assess their accuracy and validity, and we found that the relative error (E_r) for w_{max} between the analytical and numerical results is less than 0.336%, which indicates the FEM converges well with the analytical model based on our results.

Conflict of interest: The author declares no conflicts of interest to report regarding the present study.

Abbreviations

BT	Bulge test
NRD	Nano rectangular diaphragm
NEMS	Nano Electro Mechanical Sensors
BFRP	Basalt fiber reinforced polymer
FEM	Finite element model
PDE	Partial differential equation
CLPT	Classical Laminated Plate Theory
PAA	Polyacrylic acid
AFM	Analyzed via Atomic force microscopy
SNFs	Sub-nanometer fibers
μ	The nonlocal parameter
∇^2	Laplacian operator in two-dimensional Cartesian coordinate system
E_r	Relative error
P	Pressure
a	The diaphragm length
b	The diaphragm width
h_o	The diaphragm thickness
$w(x, y, z)$	The diaphragm deflection
w_o	The transverse deflection
u_o	The displacement at x direction
v_o	The displacement at y direction
M_x, M_y, M_{xy}	The moments of bending and twisting
Q_x, Q_y	The shear forces
σ_x, σ_y, τ_{xy}	The stresses
ε_x, ε_y	The strain
γ_{xy}	The thickness strain
ρ	The density per unit area of the diaphragm
R	The radius of curvature
D_{ij}	The diaphragm's flexural rigidity
$\bar{Q}_{ij}$	The stiffness coefficient

$\overline{N}_x$, $\overline{N}_y$ and $\overline{N}_{xy}$	In-plane force
σ_0	The biaxial residual stress per unit length
w_{max}	The Maximum deflection
E_1, E_2, E_3	The elastic modulus in the '1', '2' and '3' directions respectively
G_{12}, G_{23}, G_{13}	The shear modulus in the '1-2', '2-3' and '1-3' planes respectively
ν_{12}, ν_{23}, ν_{13}	The Poisson's ratio in the '1-2', '2-3' and '1-3' Planes respectively
E_a	The absolute error
E_r	The relative error
ξ	The value of Tsai-Wu damage criterion
C_{xy}, C_{yz}, C_{xz}	The coupling coefficient for Tsai-Wu theory
$\sigma_x, \sigma_y, \sigma_z$	The local stress components in directions (x), (y), and (z)
$\sigma_{xy}, \sigma_{yz}, \sigma_{xz}$	The local shear components
$\sigma_{xt}^f, \sigma_{yt}^f, \sigma_{zt}^f$	The local tension and compression strength components in directions (x), (y), and (z)
$\sigma_{xc}^f, \sigma_{yc}^f, \sigma_{zc}^f$	The local shear strength component
F_x , F_y	The local strength components in directions (x) and (y), respectively
F_{xy}	The local shear strength component.

Appendix A

Appendix A.1. Formulation

Appendix A.1.1. Local elasticity theories

When it comes to using nanostructures in things like MEMS and NEMS devices, stability analysis is pretty crucial. There's already some research out there looking into continuum models for the buckling of carbon nanotubes and similar micro- or nanobeam structures [47–51]. In quite a few of these studies, including one by Peddieson et al. [52], they suggest that we should apply Eringen's [53,54] nonlocal elasticity theory in these models to better predict how these structures will buckle. This is mainly because nanostructures are affected by their scale. Gibson et al. [55] have emphasized how important it is to accurately predict the characteristics of these nanostructures. If we're curious about nonlocal theories related to bending, buckling, and vibrations in beams, Reddy's work is a noteworthy reference [56,57].

In traditional local elasticity theories, the stress at a specific point is determined solely by the strain at that same point. On the flip side, nonlocal elasticity theories suggest that the stress at a given point actually relies on the strains from all points within the material. As Eringen [53,54] points out, the way a Hookean solid behaves when considering nonlocal effects can be expressed with this differential constitutive relation:

$$(1 - \mu\nabla^2)\sigma = t \tag{A1}$$

where, μ is the nonlocal parameter, and t is the macroscopic stress tensor at a point which is related to strain by generalized Hooke's law

$$\mathrm{t}(x) = S(x){:}\,\varepsilon(x) \tag{A2}$$

Here, S represents the fourth-order elasticity tensor, and the symbol $':'$ refers to the double dot product. It's clear that the nonlocal characteristics of the problem stem from the constitutive relations. Importantly, the principle of virtual work stands separate from these relations, which allows us to use it in deriving the equilibrium equations for nonlocal plates.

Appendix A.1.2. The governing PDE

A standard x, y, z coordinate system, as shown in **Figure 3**, The governing PDE of the study diaphragm subjected to uniform pressure load are become:

$$D_{11}\frac{\partial^4 w_o}{\partial x^4}+2(D_{12}+2D_{66})\frac{\partial^4 w_o}{\partial x^2\partial y^2}+D_{22}\frac{\partial^4 w_o}{\partial y^4}+\mu\overline{N}_X\frac{\partial^2 w_o}{\partial x^2}+\mu\overline{N}_Y\frac{\partial^2 w_o}{\partial y^2}+\rho\frac{\partial^2 w_o}{\partial t^2}=P \tag{A3}$$

OR in contraction form:

$$D_{11}W_{xxxx}+2(D_{12}+2D_{66})W_{xxyy}+D_{22}W_{yyyy}+\mu\overline{N}_XW_{xx}+2\mu\overline{N}_{XY}W_{xy}+\mu\overline{N}_YW_{yy}+\rho\,W_{tt}=P \tag{A4}$$

where: $D_{ij}=\frac{1}{3}\frac{h^3(y)}{h_o^3}\sum_{k=1}^{n}\left[(\overline{Q}_{ij})\right]_k(h_{ok}^3-h_{ok-1}^3),\ i,j=1,2,3,.........$

For steady state condition $\frac{\partial^2 w_o}{\partial t^2}=0$, Equation (A4) will take the form:

$$D_{11}W_{xxxx}+2(D_{12}+2D_{66})W_{xxyy}+D_{22}W_{yyyy}+\mu\overline{N}_XW_{xx}+2\mu\overline{N}_{XY}W_{xy}+\mu\overline{N}_YW_{yy}=P \tag{A5}$$

For pre-stressed rectangular thin plate in the hydraulic bulge system the in-plane Load are in x and y direction only i.e. $\overline{N}_{XY}=0$. Thus, the governing PDE (A5) are become:

$$D_{11}W_{xxxx}+2(D_{12}+2D_{66})W_{xxyy}+D_{22}W_{yyyy}+\mu\overline{N}_XW_{xx}+\mu\overline{N}_YW_{yy}=P \tag{A6}$$

By divided the Equation (A6) by D_{22} and introducing the following constants:

$$\psi_1=\frac{D_{11}}{D_{22}},\ \psi_2=\frac{(D_{12}+2D_{66})}{D_{22}},\ \alpha_1=\frac{\overline{N}_X}{D_{22}},\ \alpha_2=\frac{\overline{N}_Y}{D_{22}},\ \overline{P}=\frac{P}{D_{22}}$$

Equation (A6) will take the form:

$$\psi_1W_{xxxx}+2\psi_2W_{xxyy}+W_{yyyy}+\mu\alpha_1W_{xx}+\mu\alpha_2W_{yy}=\overline{P} \tag{A7}$$

If you move the right side of Equation (A7) over to the left side, it'll look like this:

$$\psi_1W_{xxxx}+2\psi_2W_{xxyy}+W_{yyyy}+\mu\alpha_1W_{xx}+\mu\alpha_2W_{yy}-\overline{P}=0 \tag{A8}$$

Appendix A.1.3. Levy's solution of the governing PDE

Levy proposed that the solution of Equation (A8) should be broken down into complementary, w_h; and particular, w_p, components. Each of these components can be represented by a single Fourier series, with unknown functions derived from the given boundary conditions (B.Cs). So, we can express the solution like this:

$$w_o=w_h+w_P \tag{A9}$$

Consider a plate with opposite edges, $x = 0$ and $x = a$, clamped edges, and two remaining opposite edges, $y = \pm b/2$, which may have arbitrary supports. The B.Cs on the clamped edges are:

$$\begin{aligned} &w_o=0\Big|_{x=0,a} \quad ,\frac{\partial w_o}{\partial x}=0\Big|_{x=0,a} \\ &w_o=0\Big|_{y=\pm\frac{b}{2}} \quad ,\frac{\partial w_o}{\partial y}=0\Big|_{y=\pm\frac{b}{2}} \end{aligned} \tag{A10}$$

The complementary solution is taken to be:

$$w_h = \sum_{m=1}^{\infty} f_m(y)\sin\left(\frac{m\pi x}{a}\right) \tag{A11}$$

The function $f_m(y)$ depends solely on y, while w_h meets the B.Cs outlined in Equation (A10). If we substitute Equation (A11) into Equation (A8) and use the characteristic exponent values we've found, we can express the solution of the homogeneous equation as an exponential function:

$$f_m(y) = A'_m e^{m\pi y/a} + B'_m e^{-m\pi y/a} + \frac{m\pi y}{a}\left(C'_m e^{m\pi y/a} + D'_m e^{-m\pi y/a}\right) \tag{A12}$$

Or in hyperbolic functions:

$$f_m(y) = A'_m e^{m\pi y/a} + B'_m e^{-m\pi y/a} + \frac{m\pi y}{a}\left(C'_m e^{m\pi y/a} + D'_m e^{-m\pi y/a}\right) \tag{A13}$$

The version in Equation (A13) is easier to work with for calculations. On the other hand, the solution from Equation (A11) can be expressed as:

$$w_h = \sum_{m=1}^{\infty}\left[A_m \sinh\left(\frac{m\pi y}{a}\right) + B_m \cosh\left(\frac{m\pi y}{a}\right) + \frac{m\pi y}{a}\left(C_m \sinh\left(\frac{m\pi y}{a}\right) + D_m \cosh\left(\frac{m\pi y}{a}\right)\right)\right]\sin\left(\frac{m\pi x}{a}\right) \tag{A14}$$

where the constants A_m, B_m, C_m and D_m are obtained from the B.Cs on the edges $y = \pm b/2$.

The particular solution, w_P, in Equation (A9), can also be expressed in a single Fourier series as:

$$w_P(x, y) = \sum_{m=1}^{\infty} g_m(y)\sin\left(\frac{m\pi x}{a}\right) \tag{A15}$$

The pressure (lateral distributed) load $P(x, y)$ is taken to be the following:

$$P(x, y) = \sum_{m=1}^{\infty} P_m(y)\sin\left(\frac{m\pi x}{a}\right), \tag{A16}$$

Here, we're looking at coefficients that need to be figured out $P_m(y)$. It's pretty straightforward to see that the formula for specific deflections in Equation (A15) meets the required B.Cs laid out in Equation (A10).

When we plug Equations (A15) and (A16) into Equation (A8) and work through some derivatives, we end up with a particular solution that looks like this:

$$\therefore\ w_P(x, y) = \frac{4\bar{P}a^4}{\pi^5}\sum_{m=1,3,5,\cdots}^{\infty}\frac{\pi^2}{\left(\psi_1\pi^2 m^5 - \alpha_1 m^3 a^2\right)}\sin\left(\frac{m\pi x}{a}\right) \tag{A17}$$

Combining Equations (A17) and (A14), we obtain:

$$\begin{aligned} w_o = \mu \sum_{m=1,3,5,\cdots}^{\infty}\Bigg[& A_m \sinh\left(\frac{m\pi y}{a}\right) + B_m \cosh\left(\frac{m\pi y}{a}\right) + \frac{m\pi y}{a}\left(C_m \sinh\left(\frac{m\pi y}{a}\right)\right. \\ & \left. + D_m \cosh\left(\frac{m\pi y}{a}\right)\right) + \frac{4\bar{P}a^4}{\pi^3\left(\psi_1\pi^2 m^5 - \alpha_1 m^3 a^2\right)}\Bigg]\sin\left(\frac{m\pi x}{a}\right) \end{aligned} \tag{A18}$$

Given how the B.Cs and the loads are set up, we can say that the plate's deflection will be symmetrical around the x axis, i.e., $w_o(x, y) = w_o(x, -y)$. This works with Equation (A14) if we let $A_m = D_m = 0$. So, when we put together Eqs. (A14) and (A17), we get:

$$w_o = \mu \sum_{m=1,3,5,\cdots}^{\infty} \left[B_m \cosh\left(\frac{m\pi y}{a}\right) + C_m \frac{m\pi y}{a}\sinh\left(\frac{m\pi y}{a}\right) + \frac{4\overline{P}a^4}{\pi^3\left(\psi_1\pi^2 m^5 - \alpha_1 m^3 a^2\right)}\right]\sin\left(\frac{m\pi x}{a}\right) \tag{A19}$$

where the constants B_m and C_m are obtained from the B.Cs on the edges at $y = \pm b/2$.

Equation (A19) perfectly meets the requirements of Equation (A8) as well as the B.Cs stated in Equation (A10) at $x = 0$ and $x = a$. Here are the other B.Cs that we need to consider:

$$w_o = 0\Big|_{\pm b/2} \quad , \frac{\partial w_o}{\partial y} = 0\Bigg|_{\pm b/2}$$

We can obtain the constants A_m , B_m , C_m and D_m exactly satisfy Equation (A19) and the B.Cs of clamped edges are:

$$A_m = 0, \quad B_m = -\gamma_m\left[\left(\frac{\phi_m \tanh^2(\phi_m)}{(\phi_m \cosh(\phi_m) + \sinh(\phi_m) - \phi_m \tanh(\phi_m)\sinh(\phi_m))}\right) + \frac{1}{\cosh(\phi_m)}\right],$$

$$C_m = \frac{\gamma_m \tanh(\phi_m)}{(\phi_m \cosh(\phi_m) + \sinh(\phi_m) - \phi_m \tanh(\phi_m)\sinh(\phi_m))}, \qquad D_m = 0.$$

where: $\phi_m = \dfrac{m\pi b}{2a}$, $\gamma_m = \dfrac{4\overline{P}a^4}{\pi^3\left(\psi_1\pi^2 m^5 - \alpha_1 m^3 a^2\right)}$

The deflection of the plate surface, Equation (A19), may thus be expressed:

$$\begin{aligned} w_o = \mu \sum_{m=1,3,5,\cdots}^{\infty} \gamma_m & \left[\left(\frac{-\phi_m \tanh^2(\phi_m)}{(\phi_m \cosh(\phi_m) + \sinh(\phi_m) - \phi_m \tanh(\phi_m)\sinh(\phi_m)))} - \frac{1}{\cosh(\phi_m)}\right)\cosh\left(\frac{2\phi_m y}{b}\right)\right. \\ & \left. + \left(\frac{\tanh(\phi_m)}{(\phi_m \cosh(\phi_m) + \sinh(\phi_m) - \phi_m \tanh(\phi_m)\sinh(\phi_m)))}\right)\left(\frac{2\phi_m y}{b}\right)\sinh\left(\frac{2\phi_m y}{b}\right) + 1\right]\sin\left(\frac{m\pi x}{a}\right) \end{aligned} \tag{A20}$$

The maximum deflection is obtained at the diaphragm center ($x = a/2$ and $y = 0$), where:

$$w_{\max} = \mu \sum_{m=1,3,5,\cdots}^{\infty} \gamma_m (-1)^{\frac{m-1}{2}}\left[\left(\frac{-\phi_m \tanh^2(\phi_m)}{(\phi_m \cosh(\phi_m) + \sinh(\phi_m) - \phi_m \tanh(\phi_m)\sinh(\phi_m)))} - \frac{1}{\cosh(\phi_m)}\right) + 1\right] \tag{A21}$$

Appendix A.1.4. laminated NRD moments and shear force

Let’s take a look at a basic parallelepiped shape cut from the diaphragm, as illustrated in **Figure 4**. We’re going to consider positive internal forces and moments acting on the nearer faces of this diaphragm element. To keep everything balanced, there have to be negative internal forces and moments acting on the opposite sides. The first subscript for these internal forces indicates the direction related to the surface normal where the force is applied. Meanwhile, the subscripts for the internal bending and twisting moments point to the stresses that generate them.

By analyzing the diaphragm element’s internal forces and moments and doing a bit of manipulation with that data, we can find the total equivalent shear forces and moments that act on the middle surface. These are what’s known as the stress resultants and stress couples. The stress resultants include shear forces labeled Q_x and Q_y, along with the bending and twisting moments denoted as M_x, M_y, and M_{xy}.

As for the bending moments and shear force in relation to displacements for the symmetric cross-ply laminate NRD, those are specified as follows:

$$\left.\begin{aligned} M_X &= -\mu\nabla^2\left(D_{11}\frac{\partial^2 w_o}{\partial x^2}+D_{12}\frac{\partial^2 w_o}{\partial y^2}\right)\\ M_Y &= -\mu\nabla^2\left(D_{12}\frac{\partial^2 w_o}{\partial x^2}+D_{22}\frac{\partial^2 w_o}{\partial y^2}\right)\\ M_{XY} &= -2\mu\nabla^2 D_{66}\frac{\partial^2 w_o}{\partial x\partial y}\end{aligned}\right\} \tag{A22}$$

$$\left.\begin{aligned} Q_X &= -\mu\nabla^2\left(D_{11}\frac{\partial^3 w_o}{\partial x^3}+(D_{12}+4D_{66})\frac{\partial^3 w_o}{\partial x\partial y^2}\right)\\ Q_Y &= -\mu\nabla^2\left(D_{22}\frac{\partial^3 w_o}{\partial y^3}+(D_{12}+4D_{66})\frac{\partial^2 w_o}{\partial x^2\partial y}\right)\end{aligned}\right\} \tag{A23}$$

Looking at **Figure 4**, we can relate the bending and twisting moments, along with the shear forces, to the stress components.

$$\begin{bmatrix} M_X \\ M_Y \\ M_{XY}\end{bmatrix} = \mu\nabla^2\int_{-\frac{h}{2}}^{\frac{h}{2}}\begin{bmatrix}\sigma_X \\ \sigma_Y \\ \tau_{XY}\end{bmatrix} z\, dz \tag{A24}$$

$$\begin{bmatrix} Q_X \\ Q_Y\end{bmatrix} = \mu\nabla^2\int_{-\frac{h}{2}}^{\frac{h}{2}}\begin{bmatrix}\tau_{XZ} \\ \tau_{YZ}\end{bmatrix} dz \tag{A25}$$

Appendix A.1.5. Laminated NRD stress-strain relations

In the same way, you can express the formulas for the plane stress components, based on Equations (A24), like this:

$$\sigma_X = \frac{12M_X}{h^3}Z\ ,\ \sigma_X = \frac{12M_Y}{h^3}Z\ ,\ \tau_{XY} = \frac{12M_{XY}}{h^3}Z \tag{A26}$$

where M_X, M_Y and M_{XY} are determined by Equations (A22), clearly the maximum stresses take place on the surfaces $Z = \pm h/2$ of the diaphragm.

Here are the stress-strain relationships for symmetrical cross-ply laminate NRD:

$$\begin{bmatrix}\sigma_X \\ \sigma_Y \\ \tau_{XY}\end{bmatrix} = \mu\nabla^2\left[\overline{Q}\right]\begin{bmatrix}\varepsilon_X \\ \varepsilon_Y \\ \gamma_{XY}\end{bmatrix} \tag{A27}$$

where: $\left[\overline{Q}\right] = [T_1]\,[Q]\,[T_2]^{-1}$ and:

$$Q_{ij} = \begin{bmatrix} Q_{11} & Q_{12} & Q_{13} \\ Q_{12} & Q_{22} & Q_{23} \\ Q_{13} & Q_{23} & Q_{66}\end{bmatrix} = \begin{bmatrix}\dfrac{E_{11}}{(1-\upsilon_{12}\upsilon_{21})} & \dfrac{\upsilon_{21}E_{11}}{(1-\upsilon_{12}\upsilon_{21})} & 0 \\ \dfrac{\upsilon_{21}E_{11}}{(1-\upsilon_{12}\upsilon_{21})} & \dfrac{E_{22}}{(1-\upsilon_{21}\upsilon_{12})} & 0 \\ 0 & 0 & G_{12}\end{bmatrix},$$

$[T_1]=[T]=\begin{bmatrix} \cos^2\theta & \sin^2\theta & 2\sin\theta\cos\theta \\ \sin^2\theta & \cos^2\theta & -2\sin\theta\cos\theta \\ -\sin\theta\cos\theta & \sin\theta\cos\theta & \cos^2\theta-\sin^2\theta \end{bmatrix}$ is the transformation matrix,

$T_2=[T]^{-1}[R]\,[R]^{-1}=\begin{bmatrix} cos^2\,\theta & sin^2\,\theta & -sin\,\theta\,cos\,\theta \\ sin^2\,\theta & cos^2\,\theta & sin\,\theta\,cos\,\theta \\ 2\,sin\,\theta\,cos\,\theta & -2\,sin\,\theta\,cos\,\theta & cos^2\,\theta - sin^2\,\theta \end{bmatrix}$,

$[R]=\begin{bmatrix} 1 & 0 & 0 \\ 0 & 1 & 0 \\ 0 & 0 & 2 \end{bmatrix}$ is the simple matrix.

The strain relations for NRHF are provided by:

$$\varepsilon_X=-z\frac{\partial^2 w_o}{\partial x^2},\quad \varepsilon_Y=-z\frac{\partial^2 w_o}{\partial y^2},\quad \gamma_{XY}=-2z\frac{\partial^2 w_o}{\partial x\partial y} \tag{A28}$$

For the bending moment M_x, M_y and M_{xy} substituting Equations (A20) and (A22) may thus be expressed:

$$\begin{aligned} M_X=\mu\sum_{m=1,3,5,\cdots}^{\infty}\Bigg[& B_m\left(D_{11}\left(\frac{m\pi}{a}\right)^2-D_{12}\left(\frac{2\phi_m}{b}\right)^2\right)\cosh\left(\frac{2\phi_m y}{b}\right)+D_{11}\left(\frac{m\pi}{a}\right)^2\gamma_m+C_m\left(D_{11}\left(\frac{m\pi}{a}\right)^2\right. \\ & \left.-D_{12}\left(\frac{2\phi_m}{b}\right)^2\right)\left(\frac{2\phi_m y}{b}\right)\sinh\left(\frac{2\phi_m y}{b}\right)-2C_m D_{12}\left(\frac{2\phi_m}{b}\right)^2\cosh\left(\frac{2\phi_m y}{b}\right)\Bigg]\sin\left(\frac{m\pi x}{a}\right) \end{aligned} \tag{A29}$$

$$\begin{aligned} M_Y=\mu\sum_{m=1,3,5,\cdots}^{\infty}\Bigg[& B_m\left(D_{12}\left(\frac{m\pi}{a}\right)^2-D_{22}\left(\frac{2\phi_m}{b}\right)^2\right)\cosh\left(\frac{2\phi_m y}{b}\right)+D_{12}\left(\frac{m\pi}{a}\right)^2+C_m\left(D_{12}\left(\frac{m\pi}{a}\right)^2\right. \\ & \left.-D_{22}\left(\frac{2\phi_m}{b}\right)^2\right)\left(\frac{2\phi_m y}{b}\right)\sinh\left(\frac{2\phi_m y}{b}\right)-2C_m D_{22}\left(\frac{2\phi_m}{b}\right)^2\cosh\left(\frac{2\phi_m y}{b}\right)\Bigg]\sin\left(\frac{m\pi x}{a}\right) \end{aligned} \tag{A30}$$

$$M_{XY}=\mu\sum_{m=1,3,5,\cdots}^{\infty}D_{66}\frac{m\pi}{a}\frac{4\phi_m}{b}\left[-B_m\sinh\left(\frac{2\phi_m y}{b}\right)-C_m\left(\left(\frac{2\phi_m y}{b}\right)\cosh\left(\frac{2\phi_m y}{b}\right)+\sinh\left(\frac{2\phi_m y}{b}\right)\right)\right]\cos\left(\frac{m\pi x}{a}\right) \tag{A31}$$

For shear force Q_x and Q_y substituting Equations (A20) and (A23) may thus be expressed:

$$\begin{aligned} \therefore Q_X=\mu\sum_{m=1,3,5,\cdots}^{\infty}\Bigg[& B_m\frac{m\pi}{a}\left(D_{11}\left(\frac{m\pi}{a}\right)^2-(D_{12}+4D_{66})\left(\frac{2\phi_m}{b}\right)^2\right)\cosh\left(\frac{2\phi_m y}{b}\right) \\ & C_m\frac{m\pi}{a}\left(D_{11}\left(\frac{m\pi}{a}\right)^2-(D_{12}+4D_{66})\left(\frac{2\phi_m}{b}\right)^2\right)\left(\frac{2\phi_m y}{b}\right)\sinh\left(\frac{2\phi_m y}{b}\right)+D_{11}\left(\frac{m\pi}{a}\right)^3\gamma_m \\ & -2C_m(D_{12}+4D_{66})\frac{m\pi}{a}\left(\frac{2\phi_m}{b}\right)^2\cosh\left(\frac{2\phi_m y}{b}\right)\Bigg]\cos\left(\frac{m\pi x}{a}\right) \end{aligned} \tag{A32}$$

$$\begin{aligned} \therefore Q_Y = \mu \sum_{m=1,3,5,\cdots}^{\infty} \Bigg[& B_m \frac{2\phi_m}{b}\left((D_{12}+4D_{66})\left(\frac{m\pi}{a}\right)^2 - D_{22}\left(\frac{2\phi_m}{b}\right)^2 \right)\sinh\left(\frac{2\phi_m y}{b}\right) \\ & + C_m \frac{2\phi_m}{b}\left((D_{12}+4D_{66})\left(\frac{m\pi}{a}\right)^2 - D_{22}\left(\frac{2\phi_m}{b}\right)^2 \right)\left(\frac{2\phi_m y}{b}\right)\cosh\left(\frac{2\phi_m y}{b}\right) \\ & C_m\left((D_{12}+4D_{66})\left(\frac{m\pi}{a}\right)^2 \frac{2\phi_m}{b} - 3D_{22}\left(\frac{2\phi_m}{b}\right)^3 \right)\sinh\left(\frac{2\phi_m y}{b}\right) \Bigg]\sin\left(\frac{m\pi x}{a}\right) \end{aligned} \tag{A33}$$

By plugging in Equations (A28), (A30), and (A31) into Equation (A26), we can derive expressions for the plane stress components. Similarly, the formulas for those components based on Equation (A26) can be expressed in this way:

$$\sigma_X = \frac{12M_X}{h^3}Z \text{ , } \sigma_X = \frac{12M_Y}{h^3}Z \text{ , } \tau_{XY} = \frac{12M_{XY}}{h^3}Z$$

where M_x, M_y and M_{xy} are determined by Equations (A22). Clearly the maximum stresses take place on the surfaces $Z = \pm h/2$, the stress σ_x, σ_y and τ_{xy} may thus be expressed:

$$\begin{aligned} \sigma_X = \mu \sum_{m=1,3,5,\cdots}^{\infty} \frac{12}{h^3} Z \Bigg[& B_m\left(D_{12}\left(\frac{m\pi}{a}\right)^2 - D_{22}\left(\frac{2\phi_m}{b}\right)^2 \right)\cosh\left(\frac{2\phi_m y}{b}\right) + D_{12}\left(\frac{m\pi}{a}\right)^2 + C_m\left(D_{12}\left(\frac{m\pi}{a}\right)^2 \right. \\ & \left. - D_{22}\left(\frac{2\phi_m}{b}\right)^2 \right)\left(\frac{2\phi_m y}{b}\right)\sinh\left(\frac{2\phi_m y}{b}\right) - 2C_m D_{22}\left(\frac{2\phi_m}{b}\right)^2 \cosh\left(\frac{2\phi_m y}{b}\right) \Bigg]\sin\left(\frac{m\pi x}{a}\right) \end{aligned} \tag{A34}$$

$$\begin{aligned} \sigma_Y = \mu \sum_{m=1,3,5,\cdots}^{\infty} \frac{12}{h^3} Z \Bigg[& B_m\left(D_{12}\left(\frac{m\pi}{a}\right)^2 - D_{22}\left(\frac{2\phi_m}{b}\right)^2 \right)\cosh\left(\frac{2\phi_m y}{b}\right) + D_{12}\left(\frac{m\pi}{a}\right)^2 + C_m\left(D_{12}\left(\frac{m\pi}{a}\right)^2 \right. \\ & \left. - D_{22}\left(\frac{2\phi_m}{b}\right)^2 \right)\left(\frac{2\phi_m y}{b}\right)\sinh\left(\frac{2\phi_m y}{b}\right) - 2C_m D_{22}\left(\frac{2\phi_m}{b}\right)^2 \cosh\left(\frac{2\phi_m y}{b}\right) \Bigg]\sin\left(\frac{m\pi x}{a}\right) \end{aligned} \tag{A35}$$

$$\tau_{XY} = \mu \sum_{m=1,3,5,\cdots}^{\infty} \frac{12}{h^3} Z D_{66} \frac{m\pi}{a}\frac{4\phi_m}{b}\left[-B_m \sinh\left(\frac{2\phi_m y}{b}\right) - C_m\left(\left(\frac{2\phi_m y}{b}\right)\cosh\left(\frac{2\phi_m y}{b}\right) + \sinh\left(\frac{2\phi_m y}{b}\right) \right) \right]\cos\left(\frac{m\pi x}{a}\right) \tag{A36}$$

For the strain ε_x, ε_y and γ_{xy} substituting Equations (A20) and (A28) may thus be expressed:

$$\varepsilon_X = -z\mu\left(\frac{m\pi}{a}\right)^2\left[-B_m \cosh\left(\frac{2\phi_m y}{b}\right) - C_m\left(\frac{2\phi_m y}{b}\right)\sinh\left(\frac{2\phi_m y}{b}\right) - \gamma_m \right]\sin\left(\frac{m\pi x}{a}\right) \tag{A37}$$

$$\varepsilon_Y = -z\mu\left(\frac{2\phi_m}{b}\right)^2\left[B_m \cosh\left(\frac{2\phi_m y}{b}\right) + C_m\left(\left(\frac{2\phi_m y}{b}\right)\sinh\left(\frac{2\phi_m y}{b}\right) + 2\cosh\left(\frac{2\phi_m y}{b}\right) \right) \right]\sin\left(\frac{m\pi x}{a}\right) \tag{A38}$$

$$\gamma_{XY} = -z\mu\frac{4m\pi\phi_m}{ab}\left[B_m \sinh\left(\frac{2\phi_m y}{b}\right) + C_m\left(\left(\frac{2\phi_m y}{b}\right)\cosh\left(\frac{2\phi_m y}{b}\right) + \sinh\left(\frac{2\phi_m y}{b}\right) \right) \right]\cos\left(\frac{m\pi x}{a}\right) \tag{A39}$$

Appendix B

Table A1. Failure criteria of the composite materials [9,10].

No.	Failure criteria	Mathematical formula
1	Max. stress	$\sigma_x = F_x$, $\sigma_y = F_y$, $\sigma_{xy} = F_{xy}$

2	Max. strain	$\sigma_x = F_x + \upsilon_{xy}\sigma_y$, $\sigma_y = F_y + \upsilon_{xy}\frac{E_y}{E_x}\sigma_x$, $\sigma_{xy} = F_{xy}$
3	Tsai-Wu	If the criterion used is the “strength index”: $\xi = A + B$ And if the criterion used is the inverse of the “strength ratio”: 1. $\xi = 1.0/\left(-\frac{B}{2A} + \sqrt{(B/2A)^2 + 1.0/A}\right)$ where: ξ = value of Tsai-Wu failure criterion: 2. $A = -\frac{(\sigma_x)^2}{\sigma_{xt}^f\sigma_{xc}^f} - \frac{(\sigma_y)^2}{\sigma_{yt}^f\sigma_{yc}^f} - \frac{(\sigma_z)^2}{\sigma_{zt}^f\sigma_{zc}^f} + \frac{(\sigma_{xy})^2}{\left(\sigma_{xy}^f\right)^2} + + \frac{(\sigma_{yz})^2}{\left(\sigma_{yz}^f\right)^2} + \frac{(\sigma_{xz})^2}{\left(\sigma_{xz}^f\right)^2} + \frac{C_{xy}\sigma_x\sigma_y}{\sqrt{\sigma_{xt}^f\sigma_{xc}^f\sigma_{yt}^f\sigma_{yc}^f}} + \frac{C_{yz}\sigma_y\sigma_z}{\sqrt{\sigma_{yt}^f\sigma_{yc}^f\sigma_{zt}^f\sigma_{zc}^f}} + \frac{C_{xz}\sigma_x\sigma_z}{\sqrt{\sigma_{xt}^f\sigma_{xc}^f\sigma_{zt}^f\sigma_{zc}^f}}$ 3. $B = \left(\frac{1}{\sigma_{xt}^f} + \frac{1}{\sigma_{xc}^f}\right)\sigma_x + \left(\frac{1}{\sigma_{yt}^f} + \frac{1}{\sigma_{yc}^f}\right)\sigma_y + \left(\frac{1}{\sigma_{zt}^f} + \frac{1}{\sigma_{zc}^f}\right)\sigma_z$ $C_{xy}, C_{yz}, C_{xz} = x - y, y - z, x - z$, respectively.
4	Hashin Fiber and Matrix	Fiber Failure Criterion $\xi = \begin{cases} \left(\frac{\sigma_x}{\sigma_{xt}^f}\right)^2 + \frac{\sigma_{xy}^2 + \sigma_{xz}^2}{\left(\sigma_{xy}^f\right)^2} & \sigma_x > 0 \\ \left(\frac{\sigma_x}{\sigma_{xc}^f}\right)^2 & \sigma_x \leq 0 \end{cases}$ Matrix Failure Criterion 4. $\xi = \begin{cases} \left(\frac{\sigma_y + \sigma_z}{\sigma_{yt}^f}\right)^2 + \frac{\sigma_{yz}^2 - \sigma_y\sigma_z}{\left(\sigma_{yz}^f\right)^2} + \frac{\sigma_{xy}^2 + \sigma_{xz}^2}{\left(\sigma_{xy}^f\right)^2} & \sigma_y + \sigma_z > 0 \\ \frac{1}{\sigma_{yc}^f}\left(\left(\frac{\sigma_{yc}^f}{2\sigma_{yz}^f}\right)^2 - 1\right)(\sigma_y + \sigma_z) + \left(\frac{\sigma_y + \sigma_z}{2\sigma_{yz}^f}\right)^2 + \frac{\sigma_{yz}^2 - \sigma_y\sigma_z}{\left(\sigma_{yz}^f\right)^2} + \frac{\sigma_{xy}^2 + \sigma_{xz}^2}{\left(\sigma_{xy}^f\right)^2} & \end{cases}$ These criteria are employed for fatigue development, damage simulation, and stress analysis.

References

1. Altabey WA, Kouritem SallamA, Al-Moghazy MA. Apply frequency response function schemes for damage detection in composite nanoscale-pipes under transient conditions. Nano-Structures & Nano-Objects. 2024; 39: 101259. doi: 10.1016/j.nanoso.2024.101259
2. Altabey WA, Noori M, Alarjani A, et al. Nano-Delamination Monitoring of BFRP Nano-Pipes of Electrical Potential Change with ANNs. Advances in Nano Research. 2020, 9, (1), 1–13, doi: 10.12989/anr.2020.9.1.001
3. Alizada AN, Sofiyev AH. Modified Young’s moduli of nano-materials taking into account the scale effects and vacancies. Meccanica. 2010; 46(5): 915–920. doi: 10.1007/s11012-010-9349-1
4. Alizada AN, Sofiyev AH. On the mechanics of deformation and stability of the beam with a nanocoating. Journal of Reinforced Plastics and Composites. 2011:0731684411428382.
5. Alizada AN, Sofiyev AH, Kuruoglu N. Stress analysis of a substrate coated by nanomaterials with vacancies subjected to uniform extension load. Acta Mechanica. 2012; 223(7): 1371–1383. doi: 10.1007/s00707-012-0649-5
6. Jian S, Zhu J, Jiang S, et al. Nanofibers with diameter below one nanometer from electrospinning. RSC Advances. 2018; 8(9): 4794–4802. doi: 10.1039/c7ra13444d
7. Altabey WA. The Laminated Pipeline Material Delamination Identification Based on Artificial Intelligence Schemes. Advances in Machinery, Materials Science and Engineering Application X. Advances in Transdisciplinary Engineering, 2024; 58: 827–834. doi: 10.3233/atde240713
8. Altabey WA. The fatigue damage monitoring of composite pipeline based on frequency domain analysis of electrical capacitance sensor system measurements. International Journal of Lightweight Materials and Manufacture. 2025; 8(6): 779–792. doi: 10.1016/j.ijlmm.2025.06.002
9. Altabey WA. A novel framework to identify delamination location/size in BFRP pipe based on convolutional neural network (CNN) algorithm hybrid with capacitive sensors. International Journal of Lightweight Materials and Manufacture. 2025; 8(3): 393–401. doi: 10.1016/j.ijlmm.2024.12.002

10. Altabey WA. An Artificial Intelligence-Based Scheme for Structural Health Monitoring in CFRE Laminated Composite Plates under Spectrum Fatigue Loading. Structural Durability & Health Monitoring. 2025; 19(5): 1145–1165. doi: 10.32604/sdhm.2025.068922
11. Ebrahimi F, Barati MR. Dynamic modeling of a thermo–piezo-electrically actuated nanosize beam subjected to a magnetic field. Applied Physics A. 2016; 122(4). doi: 10.1007/s00339-016-0001-3
12. Ebrahimi F, Barati MR. Vibration analysis of smart piezoelectrically actuated nanobeams subjected to magneto-electrical field in thermal environment. Journal of Vibration and Control. 2016; 24(3): 549–564. doi: 10.1177/1077546316646239
13. Ebrahimi F, Barati MR. Small-scale effects on hygro-thermo-mechanical vibration of temperature-dependent nonhomogeneous nanoscale beams. Mechanics of Advanced Materials and Structures. 2016; 24(11): 924–936. doi: 10.1080/15376494.2016.1196795
14. Altabey WA, Noori M. Mathematical Modeling of BFRP Laminated Composite Double-Chamber Mufflers Based Acoustic Transmission Loss Optimization, Lecture Notes in Civil Engineering. Springer; 2024. doi: 10.1007/978-3-031-57224-1_6
15. Altabey WA, Noori M, Wu Z, et al. Effective Technique for Structures Damage Detection Based on the Structural Frequency Maps. In: Proceedings of the 5th ECCOMAS Thematic Conference on Uncertainty Quantification in Computational Sciences and Engineering (UNCECOMP 2023), Athens, Greece, 12–14 June 2023.
16. Altabey WA, Noori M, Wu Z, Deep Learning-Based Crack, Location and Area Identification for a Pipeline by The Convolutional Neural Network Based on Crack Contour Network Method. In: Proceedings of the 5th ECCOMAS Thematic Conference on Uncertainty Quantification in Computational Sciences and Engineering (UNCECOMP 2023), Athens, Greece, 12–14 June 2023.
17. Altabey WA. A comprehensive study of a long-term creep thermo-mechanical fatigue behavior monitoring of BFRP composite pipeline using electrical capacitance sensors and deep learning algorithm. International Journal of Fatigue. 2024; 184: 108277. doi: 10.1016/j.ijfatigue.2024.108277
18. Altabey WA. Improvement of Adaptive Vibration Isolators Based on Magnetorheological Elastomer Materials. Advances in Transdisciplinary Engineering. 2024; 58: 284–290. doi: 10.3233/atde240636
19. Rossi M, Lattanzi A, Barlat F, et al. Inverse identification of large strain plasticity using the hydraulic bulge-test and full-field measurements. International Journal of Solids and Structures. 2022; 242: 111532. doi: 10.1016/j.ijsolstr.2022.111532
20. Shchemelinin Y, Nelson JW, Ryan C, et al. Hydraulic bulge forming comparison of continuous and stretch broken carbon fiber prepreg laminates. Composites Part B: Engineering. 2025; 303: 112607. doi: 10.1016/j.compositesb.2025.112607
21. Shchemelinin Y, Nelson JW, Ryan C, et al. Hydraulic bulge testing to compare formability of continuous and stretch broken carbon fiber reinforced polymer composites. International Journal of Material Forming. 2023; 16(2). doi: 10.1007/s12289-023-01743-6
22. Hill R. C. A theory of the plastic bulging of a metal diaphragm by lateral pressure. The London, Edinburgh, and Dublin Philosophical Magazine and Journal of Science. 1950; 41(322): 1133–1142. doi: 10.1080/14786445008561154
23. Mellor PB. Stretch forming under fluid pressure. Mechanics and Physics of Solids. 1956; 5(1): 41–56. doi: 10.1016/0022-5096(56)90006-0
24. Chater E, Neale KW. Finite plastic deformation of a circular membrane under hydrostatic pressure-I. International Journal of Mechanical Sciences. 1983; 25(4), 219–233. doi: 10.1016/0020-7403(83)90026-7
25. Ilahi MF. Parmar A. and Mellor P.B., Hydrostatic bulging of a circular aluminum diaphragm. International Journal of Mechanical Sciences. 1981; 23: 221–227. doi: 10.1016/0020-7403(81)90047-3
26. Ilahi MF, Paul TK. Hydrostatic Bulging of a Circular Soft Brass Diaphragm. International Journal of Mechanical Sciences. 1985; 27(5): 275–280. doi: 10.1016/0020-7403(85)90017-7
27. Altabey WA. An exact solution for mechanical behavior of BFRP Nano-thin films embedded in NEMS. Advances in Nano Research. 2017; 5(4): 337–357. doi: 10.12989/anr.2017.5.4.337.
28. Storakers B. Finite plastic deformation of a circular membrane under hydrostatic pressure. International Journal of Mechanical Sciences. 1966; 8: 619–628. doi: 10.1016/0020-7403(66)90040-3
29. Ahmed M, Hashmi MSJ. Finite-element analysis of bulge forming applying pressure and in-plane compressive load", Materials Processing Technology. 1998; 77: 95–102. doi: 10.1016/S0924-0136(97)00404-4
30. Wan K, Guo S, Dillard DA. A theoretical and numerical study of a thin clamped circular film under an external load in the presence of a tensile residual stress. Thin Solid Films. 2003; 425: 150–162. doi: 10.1016/S0040-6090(02)01103-3

31. Itozaki H. Mechanical properties of composition modulated copper-palladium foils [Ph.D. Dissertation]. Northwestern University, 1982.
32. Small MK, Nix WD. Analysis of the accuracy of the bulge test in determining the mechanical properties of thin films. Journal of Materials Research. 1992; 7(6): 1553–1563. doi: 10.1557/jmr.1992.1553
33. Vlassak JJ. New experimental techniques and analysis methods for the study of mechanical properties of materials in small volumes [Ph.D. Dissertation]. Stanford University, 1994.
34. Altabey WA. The Damage Identification in Laminated Composite Plate under Fatigue Load through Wavelet Packet Energy Curvature Difference Method. Composites Part C. 2022; 9: 100304. doi: 10.1016/j.jcomc.2022.100304. doi: 10.1016/j.jcomc.2022.100304
35. Altabey WA. A study on Thermo-Mechanical Behavior of MCD through Bulge Test Analysis. Advances in Computational Design. 2017; 2(2): 107–119. doi: 10.12989/acd.2017.2.2.107
36. Jung B, Lee H, Hwang K, et al. Observation of Size Effect and Measurement of Mechanical Properties of Ti Thin Film by Bulge Test. Transactions of the Korean Society of Mechanical Engineers B. 2013; 37(1): 19–25. doi: 10.3795/KSME-B.2013.37.1.019
37. Yang L, Long S, Ma Z, et al. Accuracy analysis of plane-strain bulge test for determining mechanical properties of thin films. Transactions of Nonferrous Metals Society of China. 2014; 24(10): 3265–3273. doi: 10.1016/S1003-6326(14)63466-X
38. Zhang J, Sun Y, Li D, et al. Modeling the mechanics of graphene-based polymer composite film measured by the bulge test. Journal of Physics D: Applied Physics. 2015; 48(42): 425302. doi: 10.1088/0022-3727/48/42/425302
39. Huang AW, Lu CH, Wu SC, et al. Viscoelastic mechanical properties measurement of thin Al and Al–Mg films using bulge testing. Thin Solid Films. 2016; 618: 2–7. doi: 10.1016/j.tsf.2016.03.064
40. Suttner S, Merklein M. Experimental and numerical investigation of a strain rate controlled hydraulic bulge test of sheet metal. Materials Processing Technology. 2016; 235: 121–133. doi: 10.1016/j.jmatprotec.2016.04.022
41. Xiang Y, Chen X, Vlassak JJ. Plane-strain Bulge Test for Thin Films. Journal of Materials Research. 2005; 20(9): 2360–2370. doi: 10.1557/jmr.2005.0313
42. Altabey WA. Innovative intelligent and expert system of bridges damage identification via wavelet packet energy curvature difference method integrated with artificial intelligence algorithms. Sound & Vibration. 2025; 59(2): 2372. doi: 10.59400/sv2372
43. Altabey WA. The Advanced Structural Health Monitoring by Non-Destructive Self-Powered Wireless Lightweight Sensor. Structural Durability & Health Monitoring. 2025; 19(6): 1529–1545. doi: 10.32604/sdhm.2025.069003
44. Tabata O, Kawahata K, Sugiyama S, et al. Mechanical Property Measurements of Thin Films Using Load Deflection of Composite Rectangular Membranes. Sensors and Actuators. 1989; 20: 135–141. doi: 10.1016/0250-6874(89)87111-2
45. Vlassak JJ, Nix, WD. A new bulge test technique for the determination of Young's modulus and Poisson's ratio of thin films. 1992; 7(12): 3242–3249. doi: 10.1557/JMR.1992.3242
46. Edwards RL, Coles G, Sharpe WN. Comparison of tensile and bulge tests for thin-film silicon nitride. Experimental Mechanics. 2004; 44(1): 49–54. doi: 10.1007/bf02427976
47. Wang Q, Xu F, Zhou GY. Continuum model for stability analysis of carbon nanotubes under initial bend. International Journal of Structural Stability and Dynamics. 2005; 5(4): 579–595. doi: 10.1142/S0219455405001738
48. Sudak LJ, Column buckling of multiwalled carbon nanotubes using nonlocal continuum mechanics. Journal of Applied Physics. 2003; 94(11): 7281–7287. doi: 10.1063/1.1625437
49. Wang CM, Zhang YY, Ramesh SS, et al. Buckling analysis of micro- and nano-rods/tubes based on nonlocal Timoshenko beam theory. Journal of Physics D: Applied Physics. 2006; 39(17): 3904–3909. doi: 10.1088/0022-3727/39/17/029
50. T. Murmu, S.C. Pradhan. Buckling Analysis of Beam on Winkler Foundation by Using Mdqm And Nonlocal Theory. Journal of Aerospace Sciences and Technologies. 2023: 206–215. doi: 10.61653/joast.v60i3.2008.660
51. Li R, Kardomateas GA. Thermal Buckling of Multi-Walled Carbon Nanotubes by Nonlocal Elasticity. Journal of Applied Mechanics. 2006; 74(3): 399–405. doi: 10.1115/1.2200656
52. Peddieson J, Buchanan GR, McNitt RP. Application of nonlocal continuum models to nanotechnology. International Journal of Engineering Science. 2003; 41: 305–312. doi: 10.1016/S0020-7225(02)00210-0
53. Eringen AC. On differential equations of nonlocal elasticity and solutions of screw dislocation and surface waves. Journal of Applied Physics. 1983; 54(9): 4703–4710. doi: 10.1063/1.332803
54. Eringen AC. Nonlocal Continuum Field Theories. Springer; 2002.

55. Gibson RF, Ayorinde EO, Wen YF. Vibrations of carbon nanotubes and their composites: A review. Composites Science and Technology. 2007; 67(1): 1–28. doi: 10.1016/j.compscitech.2006.03.031
56. Reddy JN. Nonlocal theories for bending, buckling and vibration of beams. International Journal of Engineering Science. 2007; 45(2-8): 288–307. doi: 10.1016/j.ijengsci.2007.04.004
57. Reddy JN, Pang SD. Nonlocal continuum theories of beams for the analysis of carbon nanotubes. Journal of Applied Physics. 2008; 103: 023511. doi: 10.1063/1.2833431